UNIVERSITY OF CALIFORNIA SAN DIEGO

Mechanisms of Leukocyte Migration: An Investigation of Motility in 3-Dimensional Environments

A dissertation submitted in partial satisfaction of the
requirements for the degree
Doctor of Philosophy

in

Bioengineering

by

Joshua François

Committee in charge:

Professor Juan Lasheras, Chair
Professor Shu Chien, Co-Chair
Professor Juan Carlos del Alamo
Professor Richard Firtel
Professor Klaus Ley

2018

The dissertation of Joshua François is approved, and it is acceptable in quality and form for publication on microfilm and electronically:

_____

_____

_____

_____
Co-Chair

_____
Chair

University of California San Diego

2018

DEDICATION

To James, Marie and Alex.

TABLE OF CONTENTS

LIST OF FIGURES

LIST OF TABLES

ACKNOWLEDGEMENTS

First and foremost, I would like to thank my parents James and Marie. You've both made tremedous sacrifices in your lives for me to be where I am and I'll always be greatful for everything you've done to help me succeed. Without question, I would not be here if it were not for you. I'd like to thank Alex for inspiring me to be the best role model I can possibly be. I'd also like to thank all of my aunts, uncles, and cousins for playing an important part in my growth as a person from the time I was born until now. You're all in my mind and heart regardless of how far I am from all of you.

I'd like to thank my academic mentors for all of the training you've given me throughout my undergraduate and graduate careers. Everything I've accomplished thus far has been possible because of the time, energy, and effort that you've put into me. I hope to continue my academic development and make you all proud.

Finally, I'd like to thank all of my non-academic mentors. You have all played an extremely important role in my success and you've also been the inspiration for me to dedicate my life to helping students like myself acheive success in the world of scientific research. I will never forget any of you and my dream is to continue the kind of work that you've dedicated your lives to in order to aid in the development of the next generation of scientists.

Chapters 2 and 3 are currently being prepared for submission for publication of the material. François, Joshua, Ayala, Cindy, Yeh, Yi-Ting, del Álamo, Juan Carlos, Lasheras, Juan C. The dissertation author was the primary investigator and author of this material.

VITA

2011	B. S. in Mechancial Engineering, University of Maryland, Baltimore County
2002-2007	Graduate Teaching Assistant, University of California San Diego
2018	Ph. D. in Bioengineering, University of California, San Diego

PUBLICATIONS

François, Joshua, Ayala, Cindy, Yeh, Yi-Ting, del Álamo, Juan C., Lasheras, Juan C. "Mechanics of three-dimensional neutrophil migration in extracellular environments", *In Preparation*.

Yeh, Yi-Ting, Serrano, Ricardo, François, Joshua, Chiu, Jeng-Jiann, Li, Yi-Shuan, Álamo, Juan C., Chien, S., Lasheras, Juan C. "Three-dimensional forces exerted by leukocytes and vascular endothelial cells dynamically facilitate diapedesis", *Proceedings of the National Academy of Sciences* (2017): 201717489.

Bastounis, Effie., Meili, Ruedi, Alvarez-Gonzalez, Begona, François, Joshua, del Álamo, Juan C., Firtel, Richard A., Lasheras, Juan C. "Both contractile axial and lateral traction force dynamics drive amoeboid cell motility", *J Cell Biol*, 204.6 (2014): 1045-1061.

ABSTRACT OF THE DISSERTATION

Mechanisms of Leukocyte Migration: An Investigation of Motility in 3-Dimensional Environments

by

Joshua François

Doctor of Philosophy in Bioengineering

University of California, San Diego, 2018

Professor Juan Lasheras, Chair
Professor Shu Chien, Co-Chair

Cell migration is a crucial aspect of many biological processes ranging from development, to cancer cell metastasis. One very important process is the inflammatory response, where neutrophils must migrate through a diverse set of environments as they travel from the bloodstream, across cell monolayers and through the extravascular space which contains other cells and extracellular matrix before reaching locations of injury or infection. Although many studies have focused on the biochemical and molecular signaling events involved in the entire process, little is know about the role of mechanics

in the last step, which is essentially migration through a 3-dimensional (3-D) confined environment. Extracellular matrix structure and stiffness have been shown to affect 3-D cell migration. However, it is unclear whether an optimal balance must exist between these factors for neutrophils to navigate and migrate complex 3-D environments in the presence of a chemoattractant. In the present thesis, we aim to investigate whether matrix porosity and stiffness play a determinant role in 3-D neutrophil chemotaxis. Using novel assays, imaging and computational analysis techniques, we found that although neutrophils are able to engage in directed migration in a range of matrix environments, optimal migration occurs at low densities and stiffnesses. Also, we see that these cells engage in periodic shape and motion changes that are independent of the nature of their matrix. However, unique forces are exerted on their surrounding environments in matrices with high porosities and low stiffnesses. These results demonstrate that although 3-D neutrophil migration is a robust process, the mechanical environment plays a very important role on the ability of these cells to move in 3-D spaces.

Chapter 1

Introduction

Cell migration is a fundamental process that is crucial in many physiological contexts, such as embryonic development, cancer cell migration, and inflammatory responses [1, 2, 3, 4, 5, 6]. During the different stages of embryonic development, cells must migrate to different locations in the embryo in a very coordinated manner in response to extracellular chemical stimuli [1]. During this process, cells either engage in slow, short range migration as epithelial sheets or fast, long range migration as individual mesenchymal cells. Defects in the migration of cells during embryogenesis can have consequences that range from abnormal pigmentation, heart defects, retardation and early embryonic lethality. During cancer cell metastasis, metastatic cancer cells first leave their primary tumor cite [7, 8, 9]. This is followed by intravasation into the lymph and blood systems, movement through the microvasculature, extravasation into distant tissue, and finally the establishment of a secondary tumor site.

1.1 Neutrophil migration during inflammatory responses is multi-step process

During inflammatory responses, chemokines diffuse from an initial site of injury or infection through tissue and eventually into the bloodstream, which results in the activation of a subtype of leukocytes referred to as neutrophils. Mature neutrophils are typically found in circulation and serve as the innate immune system's first responders to injury or infection [11]. After activation, these cells engage in selectin-mediated rolling along and integrin-mediated firm adhesion to the endothelium (Figure 1.1) [6, 12, 13, 14]. These cells then crawl along the endothelium before they begin to extravasate from blood vessels.

The subsequent steps that occur during inflammatory responses require the migration of neutrophils through several different physical barriers before finally reaching the initial location that incited the inflammatory response. After crawling on the endothelium, neutrophils migrate through the basement membrane, which is a thin sheet that contains extracellular matrix components such as entactin-1/nidogen-1, entactin-2/nidogen-2, laminins, heparan sulfate proteoglycans, and type IV collagen [15, 16, 17, 18]. These cells must then cross another layer of contractile cells known as the pericyte sheath, before reaching the extravascular space, which contains other cell types and extracellular matrix proteins. Once in the extravascular space, neutrophils follow the gradient of chemokines that initially incited the inflammatory response until they eventually reach the original location of injury or infection. These cells can then employ a host of tools to remedy the cause of the inflammatory response [11, 19].

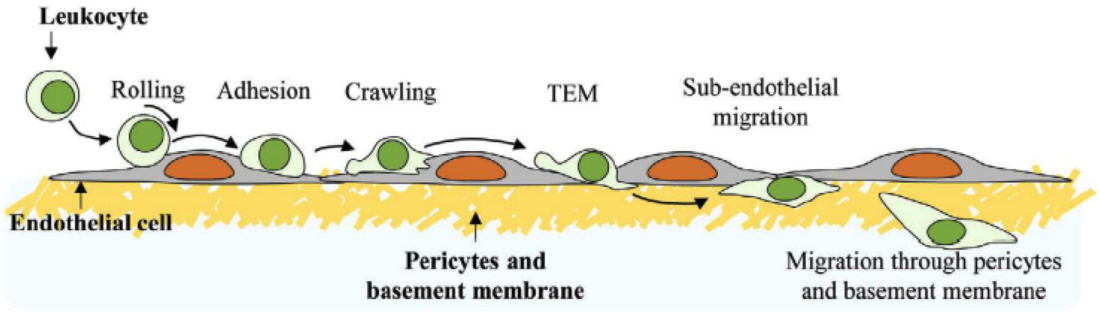

Figure 1.1: Illustration of the major steps involved during inflammatory responses. After the activation of circulating leukocytes, primarily neutrophils, these cells undergo rolling along and firm adhesion to the endothelium. Leukocytes then crawl on and migrate across the endothelium. This transmigration can occur by leukocytes squeezing between adjacent endothelial cells (paracellular transmigration) or through individual endothelial cells (transcellular migration). Leukocytes then travel across the basement membrane and the pericyte sheath. Aftrwards, these cells move through the extravascualar space before reaching the location of injury or infection that initially caused the inflammatory response [10].

1.2 Adhesion cascade involves coupling of adhesion molecules, cytoskeletal proteins and downstream signaling events

Many studies have focused on the biochemical changes and molecular signaling pathways involved in neutrophil migration during inflammatory responses. The adhesion cascade has been found to be dependent on interactions between selectins expressed on the surface of leukocytes, leukocyte intergrins, glycosalyated ligands and various cell adhesion molecules expressed on the surface of activated endothelial cells [6, 20]. During leukocyte rolling and firm adhesion, interactions between ligands and selectins further activate leukocytes and lead to downstream signaling events that include β_2 integrin activation, cytokine secretion, tyrosine phosphorylation, transcriptional activation, p38 mitogen-activated protein kinase activation, and cytoskeletal rearrangements through interactions with proteins such as ezrin, moesin, vinculin and talin [21]. The binding of

chemokines with G Protein Coupled Receptors has been shown to regulate rolling and directed leukocyte migration through pathways related to phosphatidylinositol 3-kinase (PI(3)K) γ. Extravasation has been found to involve the interaction of leukocyte integrins with endothelial cell adhesion molecules such as intercellular adhesion molecule 1 (ICAM1) and vascular cell adhesion molecule 1 (VCAM1) [6, 20]. During transmigration, transmigratory "cups" form and are believed to aid in the migration of leukocytes across the endothelium [22, 23]. Subsequent migration, which occurs in confined 3-dimensional (3-D) environments, is known to depend on the small GTPases RHOA, RAC, and CDC42 [24]. However, of the aforementioned steps, this last step is the least well understood. This is in large part due to the lack of available tools to link the known signaling pathways with the physical behavior of 3-D leukocyte migration in a systematic manner.

1.3 Quantitative methods have enabled detailed description of amoeboid locomotion

Typically, leukocyte migration has been studied in the general context of 2-dimensional (2-D) "amoeboid" migration, which is a term that desribes cells that undergo dynamic shape changes and cytoskeletal rearrangements [25, 26]. Early studies focused on amoeboid motility have involved coating glass coverslips with extracellular matrix proteins such as fibronectin or collagen and allowing amoeboid cells to adhere and migrate on the coated coverslips [27, 28, 29]. To replicate the environmental conditions that cause leukocytes to migrate during inflammatory responses, assays were used in these studies that exposed amoeboid cells to gradients of chemokines that enabled directed migration (chemoattractants). The resulting *in-vitro* experiments where these cells migrate towards a chemoatractant solution are referred to as chemotaxis assays. These assays have been the primary method for studying leukocyte migration and the

necessary signialing pathways involved.

Initial chemotaxis assays have been very useful in gaining an understanding of amoeboid migration. However, innovations in experimental and computational techniques have facilitated more quantitative investigations into the process. During 2-D migration, cells dynamically regulate new and old adhesions to their substrata, which causes traction forces to be exerted on the substrates. The resulting deformations from these forces can be observed by plating cells on soft elastic substrates coated with extracellular matrix proteins. By measuring the deformations on the substrate surface and solving the Elastostatic equation for a point load on an elastic material, the traction forces in the plane of the substrate surface caused by the cell can be calculated [30]. Ths method has been termed Traction Force Microscopy. Although this method was originally developed to study fibroblast locomotion, it has been applied to study leukocyte motility and has added quantitative details that increase our understanding of amoeboid migration. For example, a major finding from these studies has been that leukocytes tend to exert contractile stresses near their rear (uropod) during 2-D migration [31, 32, 33].

Since its initial development, Traction Force Microscopy has advanced with respect to computational time, accuracy, and the ability to compute both in-plane and out of plane traction forces [34, 35, 36]. Advanced image processing techniques have been coupled with Traction Force Microscopy to explicitly define a motility cycle for amoeboid cells (Figure 1.2) [37, 38]. This cycle involves the projection of a protrusion at the cell front, formation of a new adhesion at the front, contraction of the cell, retraction of the rear and finally relaxation of the cell. The dominant type of force that these cells exert on their environments in these assays are pulling forces during cell contractions.

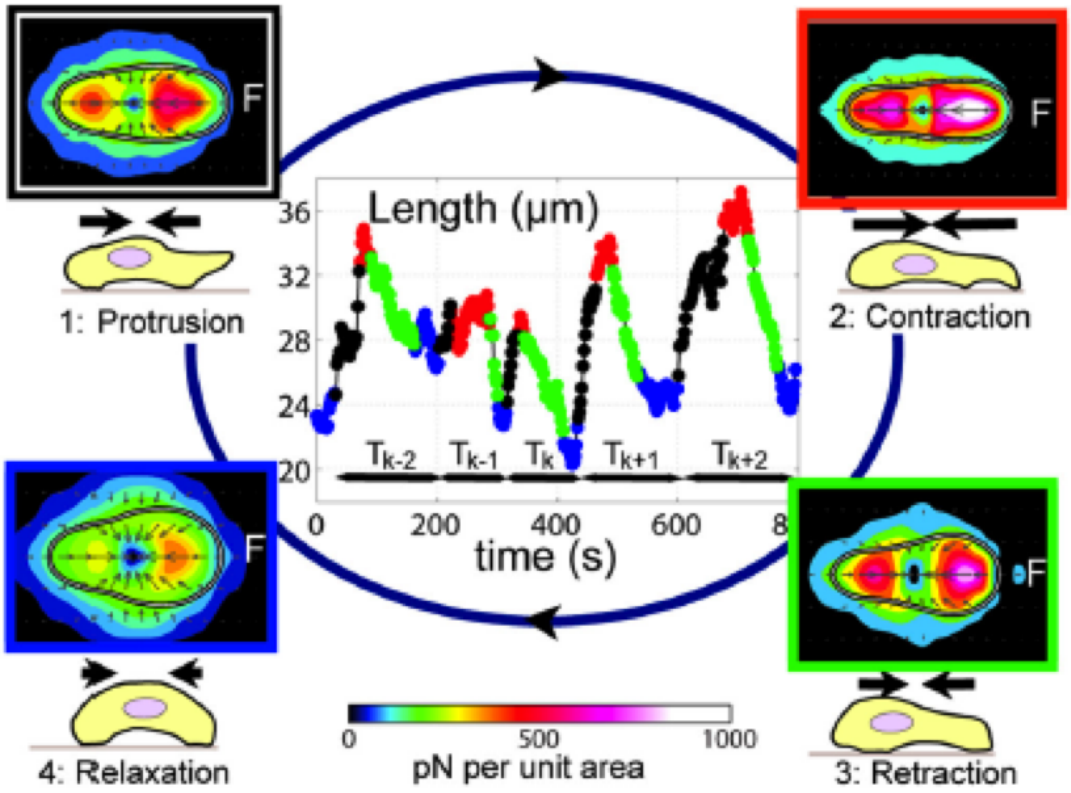

Figure 1.2: Schematic outlining the mechanical steps involved in the 2-D amoeboid cell motility cycle. A cell segmentation algorithm was used with Traction Force Microscopy to define periodic actions during *Dictyostelium discoideum* chemotaxis. The center square shows changes in cell length over the course of an experiment. The dynamics of these length changes were used to define the 4 different stages of the cell's motility cycle: protrusion (black), contraction (red), retraction (green), and relaxation (blue). Cell contour and traction stresses were phase averaged and show an increase in cell length during the protrusion stage, an increase in traction stresses during the contraction phase, a decrease in cell length during the retraction phase, and a decrease in traction stresses during the relaxation phase [37].

1.4 3-D neutrophil migration can be studied using simple *in-vitro* assays

With respect to 3-D leukocyte migration, typical experimental approaches have been either under-agarose assays, or the embedding of cells in gels comprised of reconstituted extracellular matrix proteins. Microfluidic devices with constrictions made of Polydimethylsiloxane (PDMS) have also been quite common, although the geometry and stiffness of this material are farther from what is encountered physiologically when compared to agarose or extracellular matrix gels [39, 40, 41]. Under agarose assays are performed by placing an agarose cap with two holes on a glass coverslip (Figure 1.3) [42, 43, 44]. A solution of cells is then placed in one hole and the cells are allowed to adhere to the glass coverslip while a chemoattractant solution is placed in the other hole. The chemoattractant diffuses through the agarose and causes the cells to migrate under the agarose. This assay provides full confinement for cells with their apical side remaining in contact with a soft material that can mimick the mechanical properties of material found in physiological conditions. However, the basal side of cells is still in contact with a glass coverslip, which is relatively rigid and nonphysiological.

Systems consisting of reconstituted extracellular matrix proteins are usually comprised of collagen and are fabricated by mixing solutions containing cells with solutions of reconstituted collagen [45]. When these extracellular matrix gels form, cells are fully embedded in a 3-D protein matrices. These systems can be made on glass coverslips, or inside of microfluidic devices that can help establish chemoattractant gradients and induce directed migration [46, 47, 48]. Assays based on cells embedded in extracellular matrices are ideal *in-vitro* systems, because the mechanical properties of these gels can be tuned and the gels exibit mechanical responses that are physiological [49]. However, there are currently very few analysis tools for studying migration in

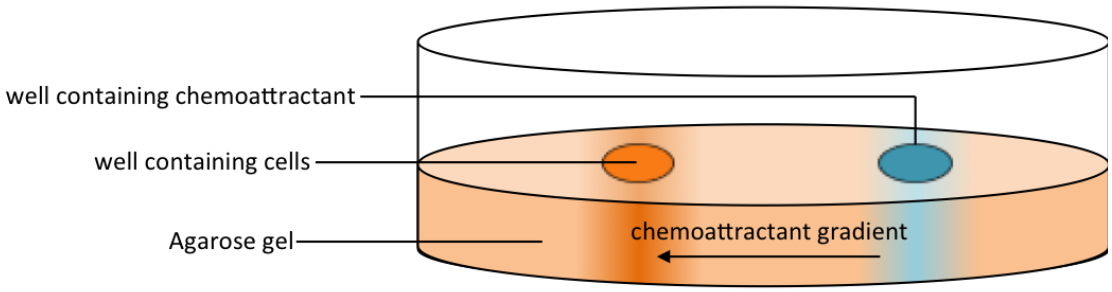

Figure 1.3: Schematic illustrating the setup of a typical under-agarose assay. The under-agarose assay was an initial means for inducing directed migration in a confined environment with stiffnesses closer to those that cells such as leukocytes typically encounter. After placing an agarose cap with two holes on a glass coverslip, cells are put in one hole and a chemoattractant solution is put in the other hole. The porosity of agarose facilitates diffusion of the chemoattractant through the gel. Cells in the other hole sense this gradient and migrate towards the chemoattractant source. Cells must migrate underneath the agarose to chemotax, thus providing full confinement during chemotaxis. However, part of this confinement is due to the rigid and non-physiological glass coverslip.

these systems that are analogous to those that are available for studying 2-D leukocyte migration.

1.5 3-D neutrophil migration regulated by push and pull forces

Under 3-D confinement, neutrophils must navigate complex environments that require shape changes regulated by actin polymerization and myosin II mediated contractility (Figure 1.3) [24]. These cells must also exert the necessary traction forces on their surrounding matrix to migrate [50]. Two major types of forces that are crucial during 3-D migration are push and pull forces. Push forces are controlled by actin polymerization and Arp 2/3 complex mediated actin branching at the front of migrating cells. Pull forces are controlled by myosin II, which localizes at the rear of leukocytes during 3-D migration. The interplay of these two types of forces can result in different modes of

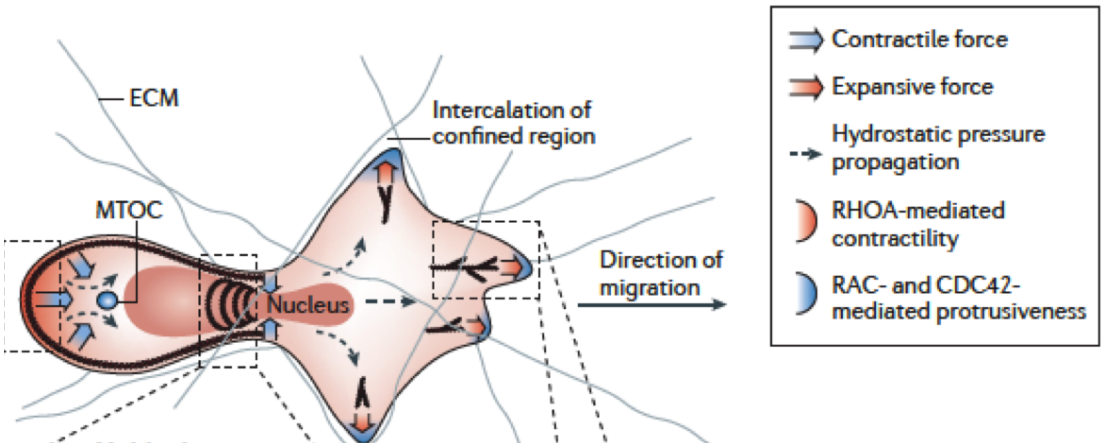

Figure 1.4: 3-D leukocyte migration is dependent on push and pull forces. These forces are generated by the interplay of actin polymerization and branching at the front of cells and myosin II mediated contraction at the rear of cells. Additionally, contractile forces may generate hydrostatic pressure gradients that cause cytoplasmic material to flow. This may result in protrusions that are a consequence of this fluid flow (blebs) as opposed to actin polymerization [50].

migration. One such mode is similar to that which is observed during 2-D amoeboid migration, which is dependent on adhesive coupling between leukocyte integrins and the extracellular environment [51]. However, it has been shown that these cells are able to migrate in 3-D spaces without the use of integrins [52]. The exact balance between push and pull forces during 3-D leukocyte migrate is currently unclear. Hypotheses include a process referred to as ”chimneying”, where cells rely on applying pressure on their surrounding environment to push off nearby physical objects. Another hypothesis involves the generatation of hydrostatic pressure gradients due to actomyosin contractility near the front or rear of the cell. This would result in cytoplasmic flow to different parts of the cell and the eventual formation of protrusions that are refered to as ”blebs” [25]. Nevertheless, the circumstances in which these different modes are used indepedently or together are still a topic of investigation.

1.6 3-D neutrophil migration regulated by push and pull forces

Under 3-D confinement, neutrophils must navigate complex environments that require shape changes regulated by actin polymerization and myosin II mediated contractility (Figure 1.3) [24]. These cells must also exert the necessary traction forces on their surrounding matrix to migrate [50]. Two major types of forces that are crucial during 3-D migration are push and pull forces. Push forces are controlled by actin polymerization and Arp 2/3 complex mediated actin branching at the front of migrating cells. Pull forces are controlled by myosin II, which localizes at the rear of leukocytes during 3-D migration. The interplay of these two types of forces can result in different modes of migration. One such mode is similar to that which is observed during 2-D amoeboid migration, which is dependent on adhesive coupling between leukocyte integrins and the extracellular environment [51]. However, it has been shown that these cells are able to migrate in 3-D spaces without the use of integrins [52]. The exact balance between push and pull forces during 3-D leukocyte migrate is currently unclear. Hypotheses include a process referred to as ”chimneying”, where cells rely on applying pressure on their surrounding environment to push off nearby physical objects. Another hypothesis involves the generatation of hydrostatic pressure gradients due to actomyosin contractility near the front or rear of the cell. This would result in cytoplasmic flow to different parts of the cell and the eventual formation of protrusions that are refered to as ”blebs” [25]. Nevertheless, the circumstances in which these different modes are used indepedently or together are still a topic of investigation.

1.7 Mechanics of extracellular environment linked to 3-D migration

The types and balance of forces that originate from internal actions of migrating leukocytes can vary and are crucial for the migration of these cells. A variable that is as important as these internal factors are the cells' surrounding environments. The extracellular matrix in extravascular spaces is diverse with respect to densities and mechanical properties [53]. For example, when comparing matrices in tissue types such as loose connective tissue and muscle tissue, the former is relatively sparse and soft while the later is relatively dense and stiff [54, 55]. Previous studies have demonstrated the importance of the mechanical environment on the robustness of 3-D migration for cells generally. Specifically, the effect of matrix density has been recently investigated in several studies related to 3-D cancer cell migration in systems with either collagen gels or matrigel. MDA-231 human breast cancer and HT-1080 fibrosarcoma cell speeds have been shown to be related to extracellular matrix concentration in a biphasic manner [56, 57]. Wu et al. also found a biphasic relation between the concentrations of matrigel with cell speed, although it is important to note that matrigel has mechanical properties that differ from collagen networks. These relationships are consistent with a computational model for 3-D cell migration that showed extracellular matrix stiffness, which increases with matrix density, and ligand density were two key factors in explaining how increasing matrix density can led to biphasic cell speeds [58].

The aforementioned 3-D cancer cell migration studies have been crucial in our understanding of 3-D cell migration. However, there are key differences between leukocytes generally and cancer cells. An important different is that leukocytes are regarded as fast moving cells, with speeds that can be an order of magnitude higher than those of cancer cells [59]. Therefore, the results obtained in studies focused on matrix density

and cell migration for cancer cells may not be directly applicable in our attempts to understand how matrix density affects neutrophil migration in 3-D spaces.

It is logical that cells must utilize their surrounding matrix material to adhere and generate sufficient forces to migrate in 3-D environments. However, the previously mentioned studies show that as the matrix material increases, the stiffness of the matrix increases and this can possibly affect the ability of cells such as luekocytes to migrate as a consequence of steric hindrance. This appears to point to competing effects and has driven the central basis of this thesis work, which is focused on investigating whether extracellular matrix structure and stiffness play a determinant role in directed 3-D neutrophil migration.

1.8 Dissertation outline

In an effort to address the hypothesis that extracellular matrix density and stiffness play a determinant role in directed 3-D neutrophil migration, it was imperative to gain novel insights into the mechanics of 3-D neutrophil migration. This in turn created a necessity for the development of new assays, technologies, and metrics for characterizing 3-D cell migration generally and 3-D neutrophil migration specifically. These efforts will be described fully in the present thesis.

The studies presented in this thesis have been explicitly separated into two main chapters. The second chapter of this thesis contains a population study of guided neutrophil migration in 3-D collagen matrices with different matrix structures and stiffnesses. A novel cell-tracking algorithm was developed and applied to experiments under low magnification to track and obtain significant statistics that describe the kinematics of 3-D neutrophil migration. The results from this study showed that although neutrophils are capable of directional migration in diverse 3-D environments with various extracellular

matrices that range from porous and soft to dense and stiff, these cells chemotax faster in environments with larger pore sizes and lower stiffnesses. Thus, extracellular matrix structure and stiffness does play a significant role in directed 3-D neutrophil migration. Results from this study also reveal that the persistence of these cells is a function of matrix structure and stiffness. Additionally, these cells exhibit long memory persistence in collagen matrices, with slow decaying correlations in the cells' velocities and persistence that are maintained over long time scales.

The second chapter is aimed at understanding how the mechanics of cell-matrix interactions can lead to robust neutrophil migration in various types extracellular environments, but optimal neutrophil chemotaxis in matrices with high porosities and low stiffnesses. In this second study, a novel cell segmentation and tracking algorithm was developed and used with a 3-D volume correlation method to characterize cell shape changes, motion, and matrix deformations during 3-D neutrophil migration. Results from this study showed that neutrophils exhibit periodicity in their shape changes and velocities during directed migration and cell shape changes are correlated with cell velocities in ways that are unique to their extracellular environment. We find that cells adopt similar cell shapes regardless of their 3-D environment. Also, neutrophils dynamically utilize push and pull forces, with pushing usually occuring near the front or entirely around cells, while possible pulling events occasionally occured near the cells' rears. This chapter is then followed by a concluding chapter which summarizes the major results and ideas presented in this thesis.

The work from these studies provides the field of neutrophil migration with new experimental and computational tools and methods to investigate the mechanics of 3-D motility in confined environments that are similar to physiological extravascular spaces. These tools and methodologies can be extended and applied to studies involving different types of cells in 3-D spaces, including cancer cells. More importantly, these studies show

that the mechanical structure and properties of 3-D environments play a crucial role in cell-matrix interactions and thus can affect how neutrophils chemotax in 3-D spaces.

Chapter 2

Population Study

2.1 Introduction

Cell migration in 3-dimensional (3-D) environments is a dynamic process that in general is highly dependent on the environment's mechanical structure and properties. In 3-D extracellular matrices, matrix material is necessary for migration. However, cell migration can be hindered if matrices are too dense, which appears to lead to competing affects. In this study, we used a custom chemotaxis chamber and a novel cell tracking algorithm to study the directed migration of neutrophil-like cells and investigate whether matrix structure and stiffness plays a determinant role in 3-D neutrophil migration. Through the analysis of the resulting cell trajectories, we found that neutrophil-like cells were able to migrate in various types of collagen matrices with pore sizes that ranged from tens of microns to sizes smaller than the diameter of the cells, and also stiffnesses from varied from 10^1-10^2 Pa. However, migration for these cells in 3-D collagen networks decreased in response to decreasing matrix porosity and increasing matrix stiffness. We also found that neutrophil-like cells migrating in 3-D collagen gels

exhibited long-memory persistence, with persistence maintained over long time scales and persistence lengths that decreased with increasing collagen gel densities. Together, these results show that although neutrophils are capable of migrating in a diverse range of extracelular matrix environments, optimal directed neutrophil migration occurs in matrices with low porosities and stiffnesses.

2.2 Materials and Methods

2.2.1 Cell culture and differentiation

Cells from the human promyelocytic leukemia cell line (HL-60, ATCC) were cultured and differentiated into neutrophil like cells (dHL-60) as previously described [60]. HL-60 cells were grown to approximately 1x10^6 cell/mL and passaged every 2-3 days in Roswell Park Memorial Institute medium (RPMI-1640, Thermo Fisher Scientific) supplanted with 1-glutamine and 10% fetal bovine serum (FBS, Omega Scientific). We differentiated HL-60 cells by taking 1.5 x 106 cells from each passage and placing them in supplanted RPMI-1640 medium with the addition of 1.3% dimethyl sulfoxide (DMSO, Sigma). We then performed experiments with dHL-60 cells 4 days after being cultured in the presence of DMSO. Both HL-60 and dHL-60 cells were incubated at 37°C and 5% CO_2.

2.2.2 *In-vitro* 3-D directed migration assay

An adapted version of a previously published custom built chemotaxis device was used to study 3-D chemotaxis (Figure 2.1A) [45]. First, 25 mm glass coverslips (Fisher Scientific) were treated on one side with 250 µL of 0.1 NaOH for 5 minutes. The NaOH was then removed and the coverslips were rinsed with distilled H $_2$ 0. The coverslips were allowed to dry and we added 1-aminopropyltriethoxysilane (APTES, Sigma) to

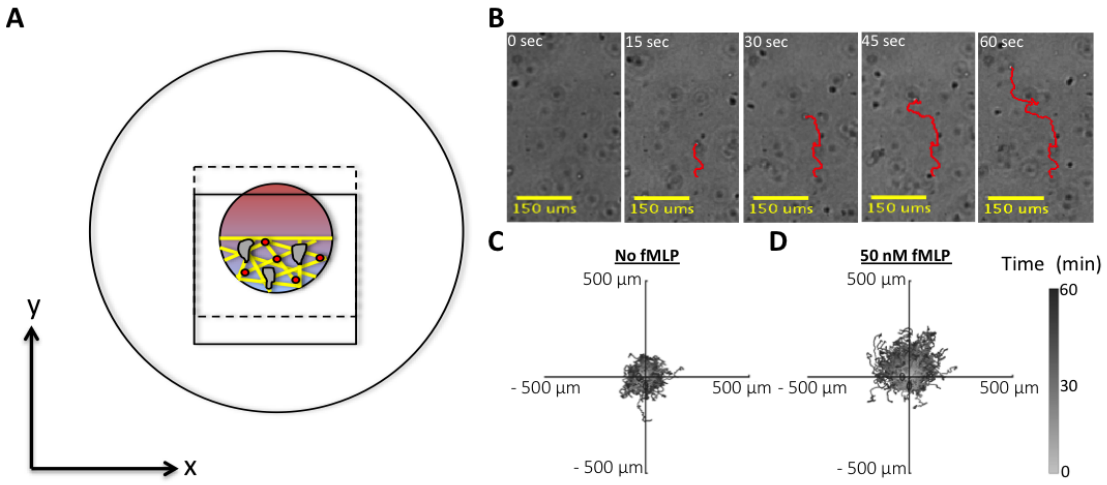

Figure 2.1: *In-vitro* assay facilitates the study of directed 3-D neutrophil migration. (A) Schematic of chemotaxis chamber containing collagen gel, embedded dHL-60 cells, fluorescent micro-beads, and fMLP above collagen gel. (B) Custom cell tracking algorithm enables the tracking of dHL-60 cells migrating towards fMLP. Representative time-lapse series of experiment with fMLP added shows one cell being tracked, whereas actual analysis is performed for many cells in each experiment. (C-D) Representative cell trajectories from experiments where either supplanted RPMI-1640 50nM fMLP solution was added above collagen gel show that fMLP induces directed migration in device. Each experiment shows trajectories for over 200 cells, and transition from light to dark gray for trajectories represent progression in cell positions over time.

their treated sides. After 30 minutes, the coverslips were rinsed again with distilled $H_2 0$ and placed on kimwipes for air dying with the treated surfaces face up.

Next, 12 mm diameter holes were punched in the center of 50 x 9 mm Falcon petri dishes (BD Falcon). A treated glass coverslip was attached to the bottom of the petri dish with its treated side face up using vacuum grease (Beckman Vacuum Grease Silicone). Another treated glass coverslip was attached to the top of the hole with its treated side face down and covering most of the hole.

2.2.3 Collagen gel fabrication

Collagen gels were fabricated by neutralizing solutions of rat tail type 1 collagen dissolved in 0.2N acetic acid (Corning) with 1N NaOH in proportions recommended by the manufacturer. A suspension of supplanted RPMI 1640 media containing $4.7x10^3$ dHL-60 cells was added instead of the recommended 10X PBS and water. A 1.2% solution of fluorescent microspheres (Molecular Probes) was also mixed with the collagen solution. While mixing the different constituents of the collagen gel, all solutions as well as a metal block that the assembled chemotaxis device rested on were placed in a small container filled with ice. After the collagen gel solution was made, 113 µL of the solution was pipetted into the pocket of the device and placed in an incubator at 37°C and 5% CO_2 for 30 minutes. The chambers were placed in an incubator vertically to allow the gel solution to settle to the lower half of the 12 mm pocket of the device. After 30 minutes, 113 µL of supplanted RPMI-1640 was added to the empty half of the chemotaxis device's pocket and again placed in an incubator for 30 minutes. Before imaging, the 113 µL of supplanted RPMI-1640 was aspirated and replaced with either 113 µL of a fresh supplanted RMPI-1640 solution or a solution containing 50nM of N-formylmethionine-leucyl-phenylanine (fMLP, Sigma-Aldrich) diluted in supplanted RPMI-1640. We allowed the gels to settle for 10 minutes before imaging in case the loading of fMLP caused any bulk gel deformations.

For confocal reflection experiments, only one treated glass coverslip was attached to a 50 x 9 mm Falcon petri dish with a 12 mm diameter hole (attached to bottom of hole). Collagen gels were fabricated in the same manner as described above, with the exception of cells in the supplanted RMPI-1640 media and fluorescent microbeads. 100 µL of the gel solution was placed on top of the glass coverslip and the petri dish was put in an incubator for 30 minutes. Finally, filled with 2 mL of supplanted RPMI-1640.

2.2.4 Imaging

Brightfield images were obtained on an enclosed Leica DMI6000 B microscope with a 5x air lens at 37°C and 5% CO_2. The magnifier above the sample was retracted to generate images that made cell automated cell tracking easier. For each experiment, four planes were acquired at 200 μm spacing in each collagen gel every 30 seconds for 1 hour. Four planes were imaged as opposed to one to follow a larger number of cells and 200 μm spacing was chosen to avoid imaging redundant cells in different planes. Collagen fibers were imaged for pore size analysis using a Leica SP5 microscope in reflection mode with a 40x immersion lens and 2x zoom.

2.2.5 Pore size analysis

A bubble analysis method was used to characterize the distribution of pore sizes from reflection confocal images of collagen networks as previously described [61]. Before performing this analysis, images were preprocessed in Fiji. First, a radial intensity gradient that appeared as an artifact from our imaging system was removed by using Fiji's sliding parabaloid feature with a radius of 50 pixels under the software's background subtraction methods. Lone pixels in the images were then removed using Fiji's despeckle feature, which applies a median filter to the image. Finally, the preprocessed images were exported to Matlab to perform the bubble analysis.

The first step in the bubble anlysis routine involved loading the preprocessed images into Matlab. Each image was binarized by using a threshold equal to the mean of the image, which resulted in the segmentation of the collagen fibers. This was followed by using the *bwareaopen* function in Matlab to remove connected components that had less than 400 pixels. This further eliminated noise inside pores in our confocal reflection images. Next, Matlab's *bwdist* feature was used to obtain a distance map

of all points inside of pores (0s) and their corresponding distances to the nearest fiber segment (1s). Gaussian smoothing was then performed on the distance map with a 100 x 100 pixel^2 filter, where the standard deviation of the Gaussian function was set to 50. This smoothened spatial gradients in the distance map. Values in the distance map were then rounded to help ensure that distinct peaks would be present in the map. Finally, local maxima were itentified using *imregionalmax* with a connectivity of 4 pixels. The local maxima in the distance maps represented the centers of pores in each image. A probability density function was then constructed for all identified pores.

2.2.6 Automated 2D cell tracking, drift correction, spurious trajectory elimination and cell trajectory plots

A custom automated match filtering algorithm was developed using Matlab to track cells from brightfield images (Figure 2.2). The retraction of the magnifier on the Leica DMI6000 B microscope resulted in images in which cells that were in focus resembled the negative of the Laplacian of a Gaussian function. Therefore, after normalizing the intensities of each image and taking the images' complement, a 6 x 6 pixel^2 Laplacian of a Gaussian filter was generated and applied using Matlab's *imfilter* function for the first time-point in each plane. This resulted in an amplification of the cells' intensities with respect to background. A histogram was then generated that contained a distribution of intensity values with two peaks. The first peak corresponded to background intensities, while the second peak corresponded to cell intensities. An intensity value between the two peaks was used as a threshold for which all intensities greater than the intensity at the first peak were set to 1 and all values less than it were set to 0. Small segments due to noise in the image were removed with *bwareaopen* and clipped segments were made whole with a dilation operation. The initial centroids of

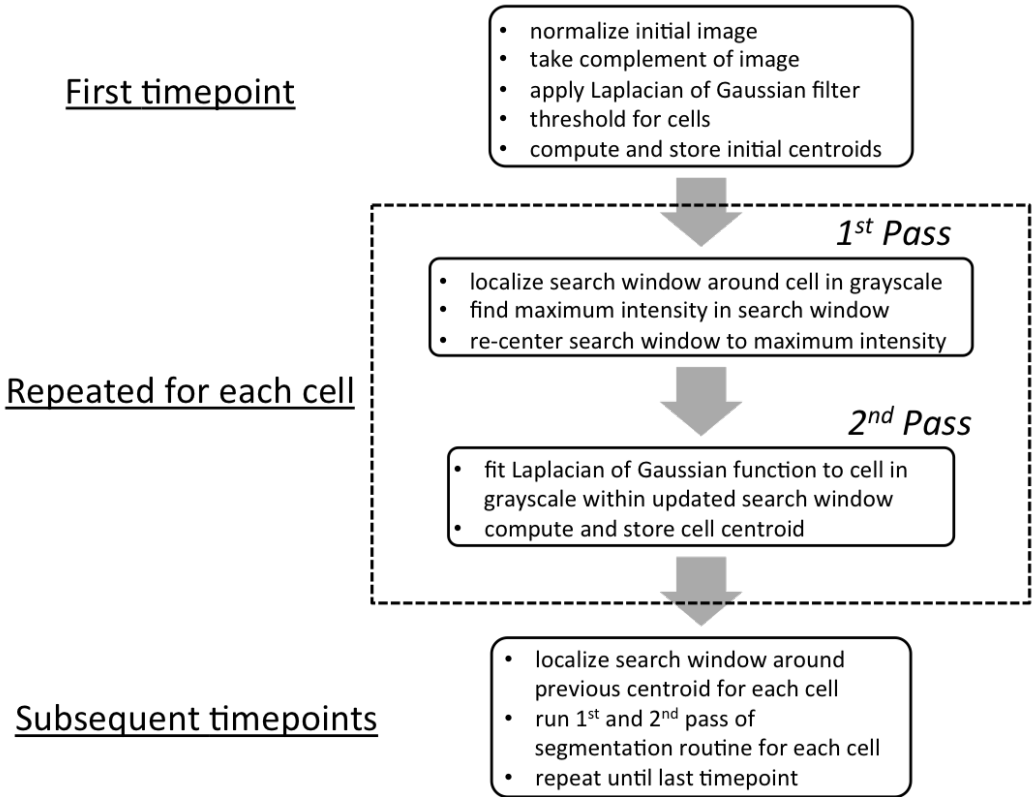

Figure 2.2: Outline of major steps performed in 2-pass tracking algorithm for population study. The first box contains the steps performed only when analyzing the first timepoint of an experiment. The second two boxes outline the 2-pass tracking that is performed for each cell after initial centroids are defined. The last box outlines the subsequent steps, which involve looking in search windows centered at centroids for each cell at the previous timepoint and performing the 2-pass tracking to find each cell's new centroid. These steps are repeated for each plane imaged and until the last timepoint.

each segmented cell were then computed using Matlab's *regionprops* function and stored. As a first pass to identify the centroid of each cell, a 10 x 10 pixel^2 search window was centered at each initial centroid in a grayscale version of the image being analyzed after the application of the Laplacian of a Gaussian filter, but before any segmentation. The maximum intensity in each window was found and the location of the maximum intesity was used to re-center the search window. A second pass to identify the centroid involved the fitting of a Laplacian of a Guassian function (Eq. 2.1) to the intensity profile of the cell in the search window.

$$LoG(x,y) = -A\left(\frac{1}{\sigma_x^2}+\frac{1}{\sigma_y^2}-\frac{(x-x_0)^2}{\sigma_x^4}+\frac{(y-y_0)^2}{\sigma_y^4}\right)e^{\left(\frac{(x-x_0)^2}{2\sigma_x^2}+\frac{(y-y_0)^2}{2\sigma_y^2}\right)} \tag{2.1}$$

In Eq. 2.1, x and y were coordinates in the search window. The coefficient A and constants σ_x and σ_y were fit parameters. The constants x_0 and y_0 were fit parameters that corresponded to the centroids of each cell. These coordinates were stored as final centroid positions, $\bar{x}$. This last step facilitated sub-pixel accuracy in centroid detection. This procedure was performed for each segmented cell.

For subsequent time-points, the same 2-pass procedure was followed after taking the complement of that image, applying a Laplacian of the Gaussian filter, and taking the complement of the resulting image. The centroid for each cell in successive search windows at the beginning of each first pass was set to the centroid identified for that cell in the previous frame. Before storing these centroids, a check was performed to ensure that cells were at least 20 pixels away from the edges of the image. If they were not, their centroids were set to the centroid values from the previous timepoint. This prevented searches for cells that may have already or would possibly leave the field of view and prevent the tracking algorithm from functioning. These steps were then repeated for the timelapse data for the other planes imaged in the collagen gel.

Drift that may have occurred during the experiment was corrected using an image correlation method that computed the shift between the first frame from the time-lapse experiment, $I_0(x, y)$, and the current image in the time-lapse experiment, $I_c(x, y)$. The Fourier transform of the natural logarithm of each image was computed using Eqs. 2.2-2.3.

$$\hat{I_0}(\xi_x, \xi_y) = ln(I_0(x, y)) \tag{2.2}$$

$$\hat{I_c}(\xi_x, \xi_y) = ln(I_c(x, y)) \tag{2.3}$$

The natural logarithm of each image was taken to enhance bright features in each image, which happened to be cells. The correlation between the first frame and current frame was computed in Fourier space (Eq. 2.4) to save computation time, since the correlation of two functions in real space reduces to the product of the two functions in Fourier space. Finally, the inverse Fourier transform of the correlation result was obtained (Eq. 2.5) and the offset in the correlation peak's coordinates from the center of the 2-D correlation map represented the drift in the current image with respect to the initial image. These offset values were subtracted from the coordinates $\bar{x}$ to correct the drift.

$$\hat{R}(\xi_x, \xi_y) = \hat{I_0}(\xi_x, \xi_y) \cdot \hat{I_c}(\xi_x, \xi_y)^* \tag{2.4}$$

$$R(x, y) = \mathcal{F}^{-1}\left\{\hat{R}(\xi_x, \xi_y)\right\} \tag{2.5}$$

Spurious cell trajectories were automatically removed. Two trajectory signatures for spurious cell tracks were encountered. First, cells that either moved too far out of the focal plane or assumed shapes that were too dissimilar from the negative of the Laplacian of a Gaussian caused the tracking algorithm to identify random points. Once a cell was lost, the tracking algorithm would continue to identify random points and this would result in object displacements that were larger than expected given the average movement

of cells in our system. A threshold of 20 pixels was chosen so that objects that had displacements equal to or greater than 20 pixels between any two successive frames were assumed to contain trajectory jumps and were automatically excluded. A second signiture was related to cells that moved too close to one another. Cells in proximity to each other sometimes appeared in the same search window. This would cause the algorithm to identify the wrong cell and continue tracking the wrong cell for the remainder of the timecourse experiment. The signature for this event would be trajectories that shared the same centroid values. Given that it would be difficult to tell which trajectory would be correct in an automated manner, any objects with the same centroid values at any timepoint/s in the timelapse data were automatically excluded.

Cell trajectories for representative experiments were plotted in Matlab using the drift corrected centroids from representative experiments. These centroid were plotted on an x-y coordinate system with their initial centroid positions being subtracted from each measured centroid position. Subsequent positions were then plotted by computing and plotting cell displacements. This enabled a visual means to compare all cell trajectories.

2.2.7 Cell speeds, velocities, chemotactic index, and maximum displacement

Cell centroids obtained from the automated tracking algorithm were used to compute cell speeds (Eq. 2.6) given n frames over 60 minutes.

$$speed = \frac{\sum_{i=1}^{n-1} \sqrt{(x_{i+1} - x_i)^2 + (y_{i+1} - y_i)^2}}{60} \tag{2.6}$$

Both x and y components of average cell velocities (Eqs. 2.7-2.8) were also computed using cell centroids for $t = 1, 2, 3, \ldots, n-1$, where n is the total number of timepoints for

each experiment.

$$v_{avg,x} = \left\langle \left\langle \frac{x(t+1) - x(t)}{\Delta t} \right\rangle_t \right\rangle_{cells} \tag{2.7}$$

$$v_{avg,y} = \left\langle \left\langle \frac{y(t+1) - y(t)}{\Delta t} \right\rangle_t \right\rangle_{cells} \tag{2.8}$$

Instantaneous velocity vectors, $\bar{v}$, were computed using Eq. 2.9 for *i and t = 1, 2, 3, . . . , n-1*. Normalized instantaneous velocity vectors, $\tilde{\bar{v}}$, were computed using Eq. 2.10.

$$\bar{v_i} = \frac{\bar{x}(t+1)) - \bar{x})t)}{\Delta t} \tag{2.9}$$

$$v_i = \frac{\bar{v_i}}{\|\bar{v_i}\|} \tag{2.10}$$

Average cell chemotaxis indices were computed by taking the cosine of an angle ϑ between a vector perpendicular to the chemoattractant gradient and the displacement vector of each cell (Eq. 2.11).

$$CI_{avg} = \langle \cos\theta \rangle_{cells} \tag{2.11}$$

Maximum displacements were computed by finding the maximum displacement traveled during a cell's trajectory over the course of an experiment.

2.2.8 Automated cell subpopulation separation

Subpopulations of cells were separated for aggregate data in each collagen gel concentration based on cell speeds. Assuming that each subpopulation was normally distributed, peaks of 1-D histograms of cell speeds were plotted and each peak was identified manually by using Matlab's *ginput* function. These initial guesses were then used with Matlab's *fit* function as initial fit parameters for fitting the sum of two gaussian functions (Eq. 2.12) with individual amplitudes A_{g1} and A_{g2}, means $x_{0,g1}$ $x_{0,g2}$, and

standard deviations $\sigma_{x,g1}$ and $\sigma_{x,g2}$. Considering that approxiamtely 97% of a normal distribution's content is contained within the distribution's mean $\pm$ 2 standard deviations [62], we established thresholds that corresponded to the highest speed of cells in the "slow moving" population and the lowest speed of cells in the "fast moving" population. These thresholds were used to separate the two populations.

$$G(x,y) = A_{g1} e^{\frac{(x-x_{0,g1})^2}{2\sigma^2_{x,g1}}} + A_{g2} e^{\frac{(x-x_{0,g2})^2}{2\sigma^2_{x,g2}}} \tag{2.12}$$

2.2.9 Mean squared displacements

Mean squared displacements (*msd*) were computed as a function of time lags, τ, using the centroids of the cells at different timepoints, t (Eq. 2.13). Mean squared displacements were computed as a function of distance lags, δ, by first computing the square of displacements at different timepoints for different lags. These squared displacements were then binned according to the distance cells travelled during the corresponding time gauge. Each bin, which represents different distance lags, was averaged in order to obtain a mean squared displacement curve as a function of δ.

$$msd\,(\tau) = \left\langle \left\langle (x\,(t+\tau) - x\,(t))^2 + (y\,(t+\tau) - y\,(t))^2 \right\rangle_t \right\rangle_{cells} \tag{2.13}$$

2.2.10 Velocity autocorrelation functions and persistence

The velocity autocorrelation function of the cells in each experiment was computed as a function of time lags τ using Eq. 2.14.

$$vac\,(\tau) = \langle \langle \tilde{\vec{v}}\,(t)\,\tilde{\vec{v}}\,(t+\tau) \rangle_t \rangle_{cells} \tag{2.14}$$

Exponential and power law correlation decay models (Eqs. 2.15-2.16) were fit to computed velocity autocorrelation functions using the built-in *fit* function in Matlab. For the power law fits, fit parameters γ_τ were used to characterize persistence in each experiment.

$$vac(\tau)_{expfit} = e^{-\frac{\tau}{\zeta_\tau}} \tag{2.15}$$

$$vac(\tau)_{plfit} = (\tau+1)^{\gamma_\tau} \tag{2.16}$$

2.3 Results

2.3.1 Custom *in-vitro* assay facilitates the study of directed leukocyte migration

We began our investigation of directed 3-D neutrophil migration and its relationship to matrix structure and stiffness by first testing the functionality of our *in-vitro* assay. Our assay was an adapted version of a design that has been utilized in several previous studies focused on 3-D directed leukocyte migration [45, 59, 63, 64]. We tested the suitability of our chemotaxis device for dHL-60 cell migration by fabricating a 0.5 mg/mL collagen gel, consisting of reconstituted rat tail type-1 collagen, fluorescent microbeads, and dHL-60 cells, which are a neutrophil-like cell line that suffucient studies have shown can be used to study neutrophil migration (Figure 2.1A) [60, 65]. We tested conditions in which supplanted RMPI-1640 was placed on top of our collagen gel in the device versus a 50nM fMLP solution. We then imaged cells in the gel for 1 hour under an inverted phase contrast microscope in brightfield mode and tracked cells using a custom automated cell-tracking algorithm (Figure 2.1B). Experiments without the addition of a chemoattractant resulted in cell trajectories emblematic of random migration, with an isotropic distribution of final cell positions (Figure 2.1C-D). Experiments that generated

these cell trajectories contained cells migrating with an average chemotactic index of approximately 0. The addition of fMLP resulted in a clear bias in migration to the positive y-direction, which is the direction towards the chemoattractant source (Figure 2.1E-F). The experiments in which a chemoattractant was added yielded a chemotaxis index of approximately 0.5, which was sufficiently high for us to conclude that our *in-vitro* assay was suitable for studying guided directed migration of our cells in collagen gels.

2.3.2 Matrix porosity decreases monotonically with increasing collagen gel density

Given that our study was focused on the relationship between matrix structure and stiffness and efficient neutrophil migration, we aimed to characterize the structure of the collagen gels that were utilized in this study. This was accomplished by first fabricating rat tail type 1 collagen gels at concentrations of 0.25, 0.5, 0.75, 1.0, and 2.0 mg/mL and imaging each gel using confocal reflection microscopy (Figure 2.2). These collagen gel concentrations were used for the population study, because the pore sizes appeared to span length scales that ranged from those comparable to the size of similar cells to orders of magnitude smaller than the size of the size [66]. Qualitatively, as collagen gel concentrations increased, we observed a decrease in the apparent pore size. We also observed that the types of fibers formed changed with increasing gel concentrations. Gels at low concentrations contained fibers that were relatively long and thin when compared to gels at higher concentrations that contained short but thicker fibers.

We quantified the pore sizes in each of these gels using the bubble analysis method (Figure 2.3), which provided distributions of pore sizes for each collagen gel concentration tested [61]. The distributions of pore sizes were significantly different from each other and mean pore size decreased monotonically as the collagen concentration increased (Figure 2.3 and Table 2.1). Interestingly, the variance in pore sizes decreased

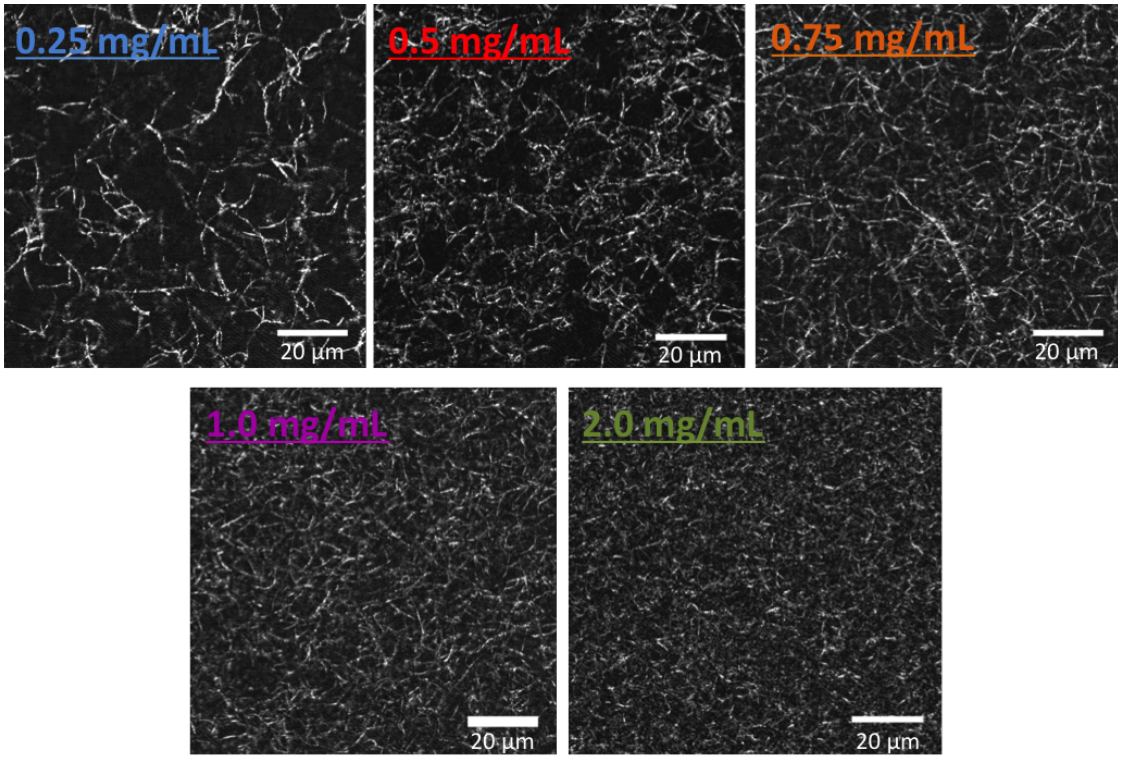

Figure 2.3: Confocal reflection microscopy images of collagen gels at various concentrations. As collagen concentration increases, matrix pore sizes span from order of magnitude similar to cell size (~20 µm) to orders to magnitude smaller than the cells ($<$ 1 µm). The types of fibers formed also changed, with long thin fibers being visible at lower concentrations and short thick fibers being visible at higher concentrations.

for increasing collagen gel concentrations, which indicated that pore diameter distributions in the collagen gels tested became more homogeneous as matrix material increased.

It is important to note that when increasing the matrix content in each gel, we not only decrease the porosity of the gels. Previous studies have shown that along with decreasing mean pore sizes, the stiffness of these gels also increases. For extracellular matrix gels at concentrations similar to those investigated in this study, gel stiffnesses increase from roughly 10^1 to 10^2 Pascals [67, 59].

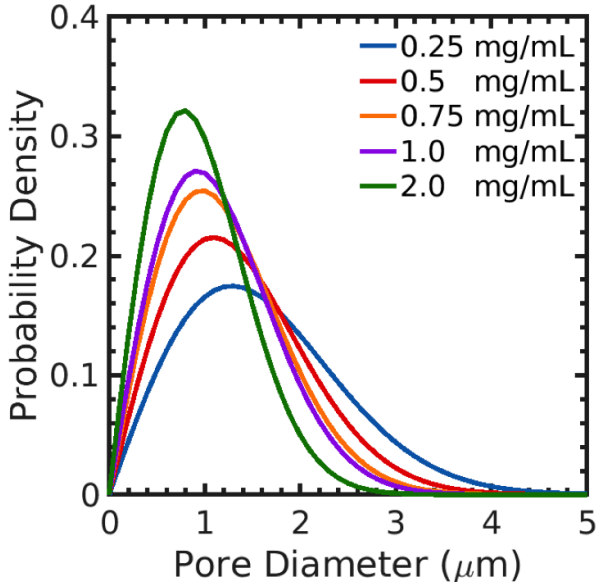

Figure 2.4: Bubble method analysis using confocal reflection microscopy images of collagen gels shows mean pore sizes decrease as collagen gel concentrations increase. Each distribution was obtained from N = 3 different gels, with at least two different locations imaged for each repeat. Kolmov-Porov test was used to test for significant differences between collagen pore size distributions.

Table 2.1: Distribution statistics from bubble analysis for each collagen gel concentration show that as collagen concentrations increased, the mean and variance of collagen pore sizes decreased. Each distribution was obtained from N = 3 different gels, with at least two different locations imaged for each repeat.

	0.25 mg/mL	**0.5 mg/mL**	**0.75 mg/mL**	**1.0 mg/mL**	**2.0 mg/mL**
mean	3.5	2.8	2.6	2.4	2.0
variance	9.3	5.2	3.0	2.6	1.7

2.3.3 Different cell speeds observed for subpopulations in 3-D collagen gels

We next decided to use simple kinematic metrics to describe cell motility in our different collagen gels. The first metric analyzed was cell speed. Although this quantity is a scalar, and therefore non-directional, it provides a general description of how cells were able to migrate in matrices with various structures and stiffnesses. To visualize this result, we constructed a 2-D probability density function of the speeds as a function of collagen gel concentrations (Figure 2.5A). We found that there appeared to be two separate subpopulations of cells in each of our gels. A "fast moving" subpopulation migrated at speeds near 7 μm/min in the lowest concentration matrices. As the concentration of the gels tested increased, the speeds of cells in this subpopulation decreased to roughly 4 μm/min. We also observed a "slow moving" subpopulation that migrated at speeds less than 1 μm/min and the speed of these cells remained low for low collagen gel concentrations and increased slightly for gels with concentrations above 0.75 mg/mL. Given that there were two different behaviors exhibited in each gel, we believed that it would be necessary to have a systematic method for separated them from each other in our analysis. To this end, we developed an automated method to distinguish the populations based on automatically determined speed thresholds (Figure 2.5B). The first threshold represents a speed for which cells that are slower than this value are grouped in the "slow moving" population, whereas cells that are faster than the second threshold are determined to be "fast moving" cells. While the "fast moving" subpopulation exhibited speeds that were comparable to values expected for amoeboid cells [38, 68], the nature of the "slow moving" subpopulation was unclear. Therefore, we decided to perform all of our analysis in this study only using cells from the "fast moving" subpopulation and results from our cell speed analysis demonstrated that neutrophils migrated faster in

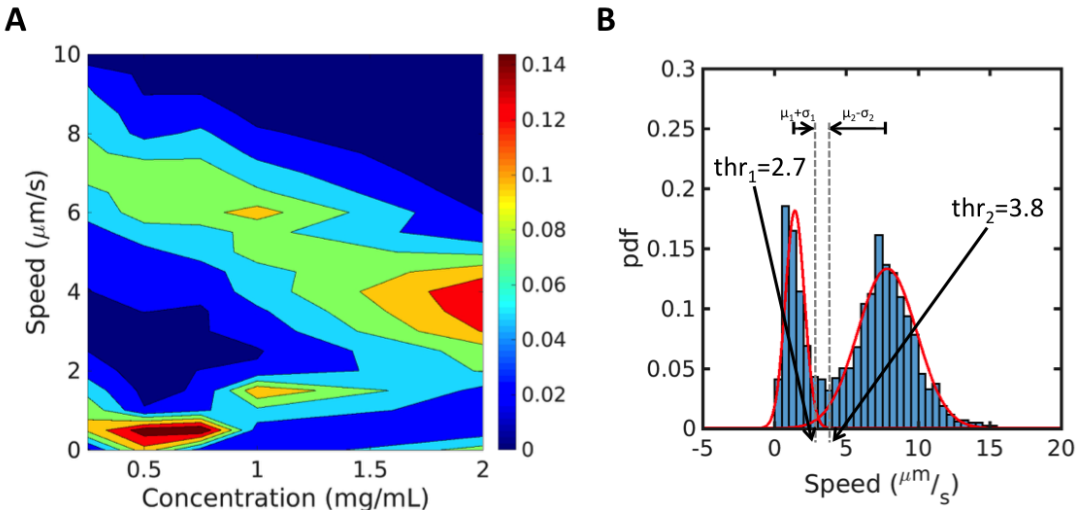

Figure 2.5: Automated separation of sub-populations observed in each collagen gel concentration tested. (A) 2-D probability density function of speed versus collagen gel concentration shows distinct "fast moving" population that decreases in speed and "slow moving" population that increases in speed with increasing matrix density. (B) Mixture model used to identify each subpopulation in collagen gels. Thresholds for each population were determined considering that 97.9% of a normal distribution contained within 2 standard deviations of the distribution's mean.

collagen gels with lower porosities and stiffnesses.

2.3.4 Chemotactic response of neutrophils in 3-D decreases with increasing collagen gel density

We next wanted to define metrics that would allow us to directly address the question of whether matrix structure and stiffness play a determinant role in efficient cell migration. These metrics would have to be related to movement in the direction of the fMLP gradient in order for us to make definitive statements about directed 3-D migration. The first such metric was the percentage of motile cells that migrated in the direction of the increasing chemoattractant gradient (y-direction) (Figure 2.6A). From this metric, we were not able to find significant differences across the different collagen gels tested. However, we did observe that over 50% of cells in each of the gels migrated towards the chemoattractant source by the end of each experiment. This indicated that dH-L60 cells

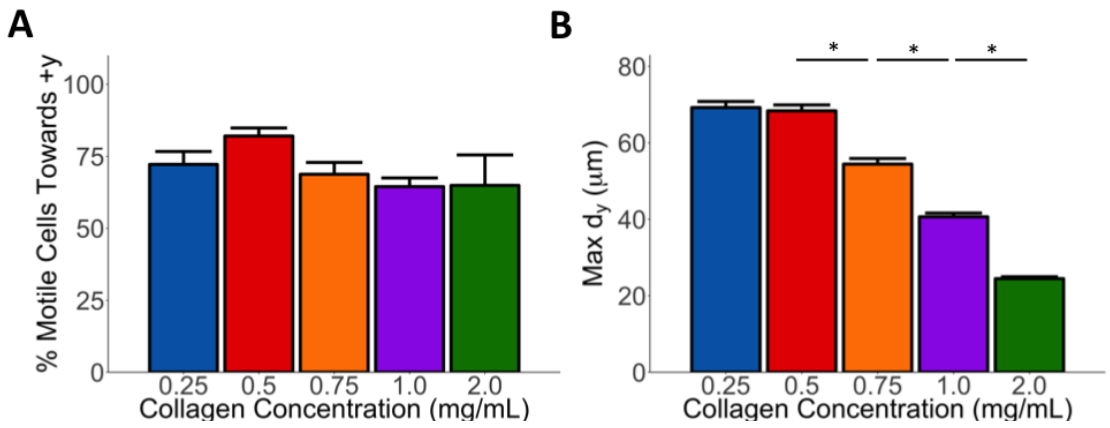

Figure 2.6: Directed 3-D neutrophil motility decreases with decreasing matrix porosity and increasing matrix stiffness. (A) No significant different in percentage of motile cells that move towards the fMLP source. However, majority of cells migrate towards fMLP source by the end of experiments. (B) Average maximum cell displacement in the direction of the chemoattractant gradient generally decreases with increasing collagen gel concentration from 0.25 mg/mL to 0.5 mg/mL. Further increases in collagen gel concentrations resulted in decreases in average directional velocities. N = 3 or more for each experiment, with at least 200 cells analyzed per repeat. Wilcoxonian rank sum test with Bonferroni correction used to test for significant differences in mean values. * $P < 0.005$.

were able to chemotax in the various extracellular matrix environments tested. We next looked at the average maximum displacement in the direction of the chemoattractant (Figure 2.6B). The maximum displacement was chosen because we observed some cells moving towards and away from the chemoattractant source during the course of experiments. The maximum displacement gave us a means to compare the strongest chemotactic response over the course of each hour long experiment. We saw that the cells were able to migrate in all of the collagen gel concentrations. From 0.25 to 0.5 mg/mL, there was no significant difference in maximum y displacements with average displacements of about 68 μm. However, these displacements significantly decreased as collagen gel concentrations increased, with an average displacement of 24.5 μm in the 2.0 mg/mL gels. This indicated that although the cells were able to migrate in environments that ranged from relatively porous and soft to relatively dense and stiff, cells were more migratory in gels with lower matrix porosities and stiffnesses.

2.3.5 Neutrophils engage in directed migration with matrix density-dependent persistent length scales

Given that directed 3-D neutrophil migration did appear to be dependent on matrix structure and stiffness, we then asked how an important aspect of directed 3-D migration such as persistence depended on these two parameters. To answer this question, we computed the mean squared displacements of cells in each of our collagen gels. When computed as a function of time lags τ, we observed that cells in all collagen gel concentrations tested had slopes greater than 1, indicating that the cells engaged in directed migration in time (Figure 2.7A, Table 2.2). However, as collagen concentrations increased, the slopes of the mean squared displacement curves decreased from 1.4 to 1.1, indicating a decreasing degree of directionality as matrix porosity decreased and matrix stiffness increased.

To gain additional insight into the dynamics of directed cell migration, we supplemented our mean squared displacement analysis as a function of time lags by also computing the mean squared displacements as a function of distance lags δ (Figure 2.7B). We saw that for short length scales, the slopes of the mean squared displacement curves were all approximately 2 (Table 2.2). However, each of the mean squared displacement curves exhibited a decrease in slope, which meant that cells eventually lost correlation in their motion at different length scales. We quantified this length scale for each mean squared displacement curve and defined it as the persistence length for cells in each gel concentration (Figure 2.8A). When plotting this persistence length for each gel concentration as a function of the mean pore diameter for respective gels, we saw that there was a direct relationship between matrix structure and stiffness and persistence length. As ECM pore sizes increased, persistence lengths increased. This told us that as cells encounter more porous and likely softer environments, their persistence length increased.

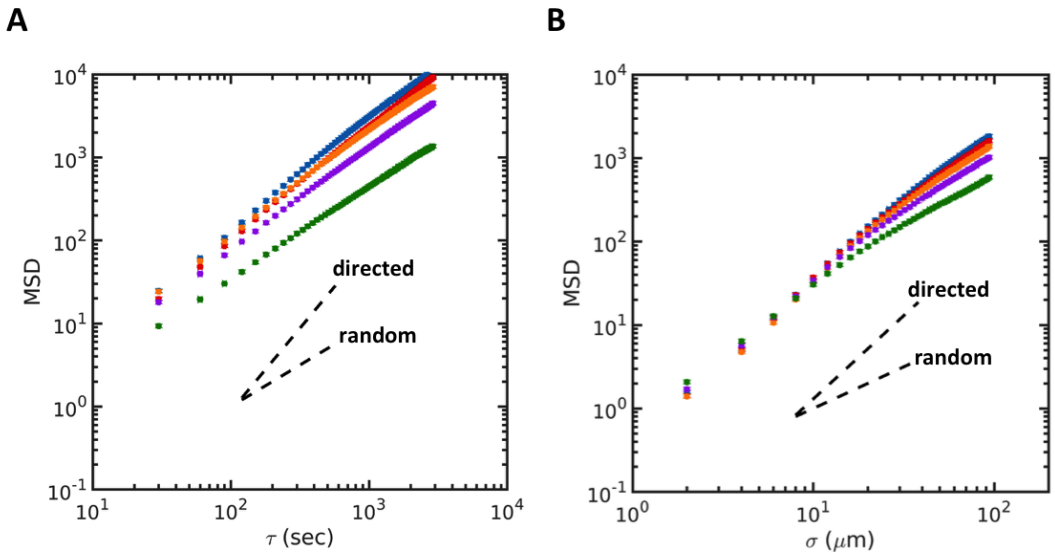

Figure 2.7: Mean squared displacements as function of time lags and distance lags illustrate directional migration of cells in all matrices tested over time and space. (A) Directional migration of cells in all gels tested, although degree of directionality decreased in gels with higher densities and stiffnesses. (B) Cells migrated with strong directionality at short length scales. Cells subsequently lost correlation in motion at different length scales. N = 3 or more for each experiment, with at least 200 cells analyzed per repeat.

Table 2.2: Slopes of mean squared displacement curves for data as function of time lags (row 1) and distance lags (row 2). Note that slopes measured in row two correspond to length scales (up to ~10 μm) in the mean squared displacement curve from Figure 6B where slopes are similar across different collagen gel concentrations.

	0.25 mg/mL	0.5 mg/mL	0.75 mg/mL	1.0 mg/mL	2.0 mg/mL
msd(τ) slope	1.4	1.3	1.3	1.2	1.1
msd(δ) slope	2	2	2	2	2

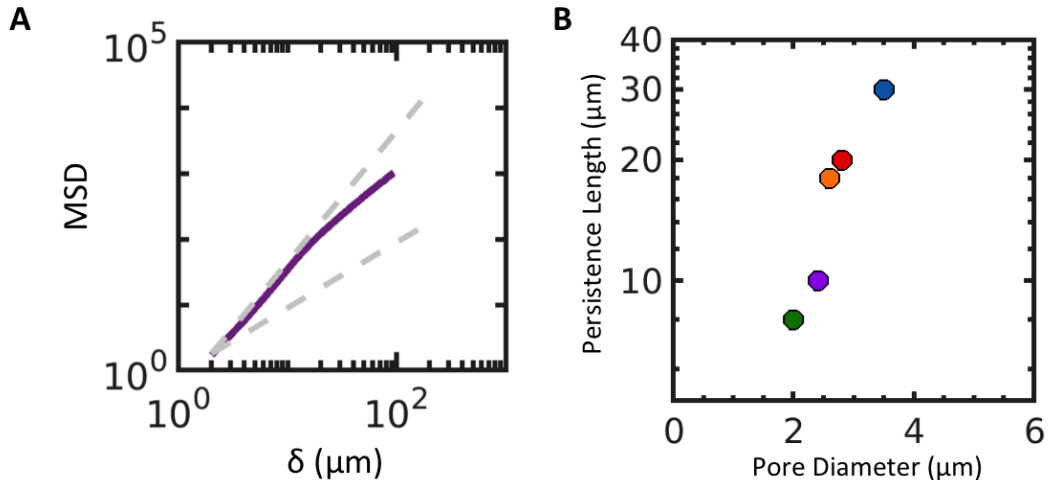

Figure 2.8: Persistence length of cells during directed migration is directly related to matrix structure, as quantified by extracellular matrix pore diameter. (A) Mean squared displacement curve for collagen gel concentration of 1 mg/mL as function of distance lags. Dashed lines with lower and higher slopes indicate slopes or 1 and 2 respectively. Mean squared displacement curve maintains slope of ~2 until roughly 10 μm. This length scale was defined as cell's persistence length in corresponding gels. (B) Dot plot showing direct relationship between persistence length and extracellular matrix pore size.

2.3.6 Neutrophils migrating in 3-D collagen gels can be described with power law decay models

To further describe the persistence of migrating neutrophils and its relation to matrix structure and stiffness, we computed the velocity autocorrelation function of the cells in each gel as a function of temporal lags (Figure 2.9A). The autocorrelation function decayed according to a power law decay model as opposed to an exponential decay model. Given the power law fit, a single fit parameter γ_τ could be used as a measure of persistence for each concentration. This parameter described how quickly the velocity autocorrelation function decayed. We found that generally γ_τ increased with increasing collagen gel concentrations (Figure 2.9B).

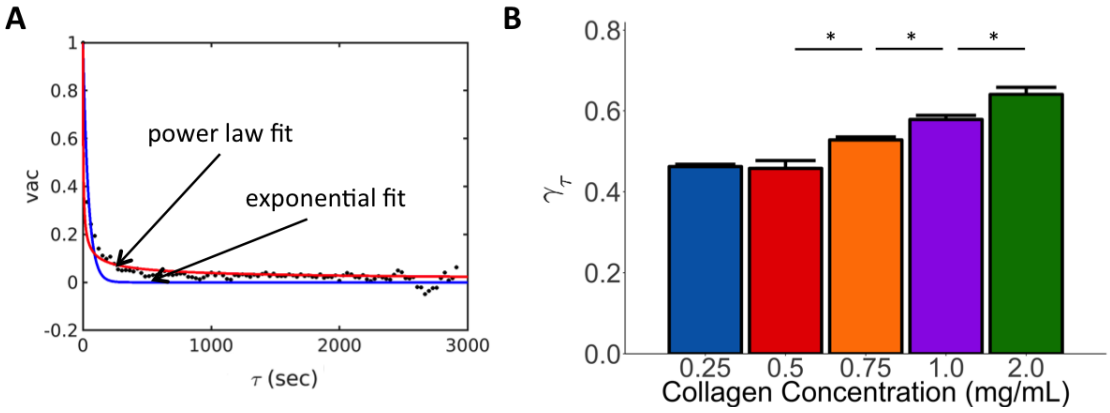

Figure 2.9: Velocity autocorrelation functions for chemotaxing dHL-60 cells decay as power law in 3-D environments, indicated that cells in these environments exhibit long memory persistence. (A) Velocity autocorrelation function for representative 0.25 mg/mL experiment can be modeled with power law decay as function of time lags. (B) Persistence, which can be characterized by fit parameter γ_τ, decreased as collagen gel concentration increased. N = 3 or more for each experiment, with at least 200 cells analyzed per repeat. Wilcoxonian rank sum test with Bonferroni correction used to test for significant differences in mean values. * $P < 0.005$.

2.4 Discussion

In this study, we were able to use a custom *in-vitro* assay to observe that during 3-D neutrophil migration, matrix structure and stiffness play a determinant role in directed migration. Changing the matrices that neutrophil-like cells were embedded inside of resulted in matrices with different structures, which were exemplified by a decreasing porosity with an increasing collagen concentrations. Pore sizes in the matrices used for this study ranged from values near the size the cells to values several orders of magnitude smaller than the cell. From published literature values, it is known that this increase in collagen concentration also resulted in an increase in matrix stiffness.

By fabricating collagen gels with a range of porosities and stiffnesses, we were able to see that the neutrophil-like cells were robust in terms of their migratory potential. The majority of cells were able to migrate towards a chemoattractant regardless of the different environments tested. This robustness is not surprising, given the fact that these cells must migrate through environments in the body that range in porosities and stiffnesses. However, we observed that in the limit of matrices tested, low collagen gel concentrations appeared to yield matrices with optimal conditions to facilitate greater chemotaxis. This was in spite of the fact that the lowest concentration matrices were relatively soft and contained pore sizes that were on orders of magnitude similar to the cells. Even in these conditions, cells were able to migrate on average at least two cell diameters.

When measuring cell persistence, which is an important characteristic related to directed migration, we saw a general decrease in directionality as cells migrated in environments that were less porous and stiffer. We also found that over short distances (¡ 10 μm), leukocytes maintained a similar type of persistence. However, as matrix pore sizes increased, their persistence length increased. This explicitely demonstrated a clear relationship between directionaly leukocyte migration and the structure of the surrounding matrix.

Our analysis showed that another metric related to persistence, the velocity auto-correlation function for neutrophils migrating in 3-D collagen gels, decayed as a power law. This result was significant because power law decays of velocity autocorrelation functions indicate that the underlying behavior of the system exhibits long memory persistence [69, 70]. This behavior describes systems in which the correlation of velocity vectors decays over time, but the decay is somewhat slow and persistence is maintained over long time scales. This describes the behavior of the neutrophil-like cells in our assay quite well. Cells are unable to maintain perfect persistent motion when migrating

in matrix like environments due to steric hindrance, and this hindrance increases as the amount of matrix material and matrix stiffness increase. However, the cells can sense the chemoattractant solution throughout the experiment. This enables them to maintain a significant degree of persistence over long time scales. In the future, the framework that stems from fields focused on long-memory persistent processes may be used to model and further understand 3-D leukocyte migration in *in-vitro* environments like ours as well as in *in-vivo* contexts.

During the course of this study, we encountered two different subpopulations in each of our gels. Although we cannot say definitively why these two subpopulations were present, we currently have two hypotheses. One hypothesis is that the presence of the "slow moving" subpopulation is an artifact of using a cell line that requires a differentiation step. It is possible that this subpopulation is a group of cells that are not fully differentiated and thus, not "neutrophil-like" cells. This may mean that the expression levels for integrins needed for cell-matrix adhesions are not high enough to enable migration in environments like the ones used in this study.

A second hypothesis is linked to the various extracellular environments used in this study. This subpopulation could possibly be fully differentiated neutrophil-like cells that are unable to migrate due to matrix porosity. Figure 2 and table 1 illustrate the heterogeneity in our collagen matrices in terms of pore sizes. Given this heterogeneity and the presence of pore sizes on length scales similar to that of the cells, some cells may be trapped inside of pores and unable to migrate. This would explain why as collagen gel porosity decreases with increasing collagen concentrations, the speed of cells in this subpopulation slightly increases. These two hypotheses could be tested by performing flow cytometry and cell sorting experiments with an anti-body targeted to a surface receptor protein such as CD11b. This receptor has been shown in previous studies to be upregulated during HL-60 cell differentiation [71]. By comparing flow cytometry

experiments using a marker for HL-60 cell differentiation with cells that have been in the presence of DMSO for 4 days, the approximate percentage of differentiated cells per dish can be estimated. During the course of this study, we found that roughly two-thirds of the dHL-60 cells in each gel condition belonged to the ”fast moving” population, while one-third belonged to the ”slow moving” population. Flow cytometry experiments would provide a baseline to check if the percentage of differentiated cells matched these proportions. Futhermore, through the use of cell sorted, cells that express CD11b at significant levels could be separated and tested in our *in-vitro* assay. If experiments with these sorted cells only produced one population, this would provide evidence that the two populations observed in our study may be a result of having both differentiated cells that can migrate robustly in our system as well as poorly differentiated cells that may not be capable of migrating in a robust manner. However, if experiments performed with sorted cells still produce the two populations that we observed, this would provide evidence that the existence of these two populations is related to the heterogeniety in the mechancial environments that the cells migrate through in our assay.

Chapter 2, in part, is currently being prepared for submission for publication of the material. François, Joshua, Ayala, Cindy, Yeh, Yi-Ting, del Álamo, Juan Carlos, Lasheras, Juan C. The dissertation author was the primary investigator and author of this material.

Chapter 3

Introduction

The study presented in chapter 2 has provided evidence that both matrix structure and stiffness play a key role in directed 3-dimensional (3-D) neutrophil migration. The study demonstrated that although neutrophils are capable of chemotaxing in 3-D environments with a range of porosities and stiffnesses, the chemotactic response of these cells is stronger in environments with high porosities and low stiffness. However, the types of cell-matrix interactions that occur in these different matrix structures and stiffnesses that enable these robust migratory behaviors is not well understood.

In this chapter, we aimed to determine how the mechanics of cell-matrix interactions leads to robust chemotaxis in a range of extracellular environments, but ultimately to optimal neutrophil migration in low density and stiffness environments. To address this, we used confocal microscopy coupled with novel technologies and metrics to describe two key aspects of cell-matrix interactions; cell shape changes & motion and push & pull forces exerted by cells on their environment [50]. To obtain a detailed description of these cell-matrix interactions, the study in this chapter was performed using high magnification imaging to characterize key metrics on a single cell level with sufficient

resolution. Results from this study showed that during directed migration, neutrophils engage in periodic cell shape changes, as well as periodic changes in their velocity magnitudes. Also, these cells correlate their shape changes with their motion. In matrices that are relatively porous and soft and matrices that are relatively dense and stiff, postive correlations exists between cell widths and motion. This is in contrast to matrices with intermediate porosities and stiffness, where a negative correlation exists between cell lengths and motion. Additionally, we found that cells explore a similar cell shape space on average, independent of the surrounding extracellular matrix's structures and stiffness. However, the deformation fields around migrating neutrophils are unique to different types of environments, with stronger deformations in matrices that have high porosities and low stiffnesses. Furthermore, we observed that migrating neutrophils dynamically exert both pulling and possibly pushing forces, which are occasionally polarized in the direction of cell polarization. Together, these results identify correlations in cell shape and motion as well as the forces that migrating neutrophils exert on matrices as possibly being related in enabling robust leukocyte migration in a range of 3-D collagen matrices, but faster chemotaxis during migration in matrices with optimal porosities and mechancial properties.

3.1 Methods

3.1.1 Cell culture, differentiation, and cytoplasmic labeling

For the single cell study, HL-60 cells were cultured and differentiated using the same protocol described in Chapter 2. Day 4 differetiated dHL-60 cells were then labeled with CellTracker Deep Red (Thermo Fisher Scientific) prior to mixing them with collagen gel solutions. Cells were incubated in a 1 nM solution of CellTracker in reconstituted RPMI-1640 without FBS for 30 minutes at 37 °C and 5% CO_2. Afterwards,

the cells were centrifuged and resuspended in the same reconstituted RMPI-1640 that was described for culturing HL-60 cells in Chapter 2.

3.1.2 *In-vitro* 3-D directed migration assay and collagen gel fabrication

The same directed migration device described in Chapter 2 (Figure 2.1A) was used for the study in this chapter. Similarly, collagen gels were fabricated in the *in-vitro* device using the same protocol for making collagen gels that was presented in the previous chapter.

3.1.3 Imaging

Imaging for the single cell study was performed on an enclosed Zeiss LSM 880 Confocal microscope under the fast Airyscan mode. A 40x water lens was use, with an additional 1.3x zoom. For experiments solely related to characterizing cell shape changes, an 80 μm stack with 0.7 μm spacing was acquired every 15 seconds. For experiments related to cell shape changes and matrix deformations, two 80 μm stacks with the same spacing were acquired every 30 seconds. The duration of timelapse experiments vaired. Each experiment was ended when a cell or cells of interest left the field of view.

Imaging volumes for experiments where only the labelled cell was imaged contained 1-2 cells in the volume, while experiments in which both the labelled cell and fluorescent microbeads were imaged only contained 1 cell. Given that dHL-60 cells are fast moving cells, we switched imaging channels for the labeled cells and labeled beads per line scan during acquisition. This was to minimize significant diffences in cell positions with respect to matrix deformation during the acquisition of the two stacks for a single timepoint.

3.1.4 Fluorescent labeling of collagen fibers

Collagen fibers were fluorescently labeled with 5-Carboxytetramethylrhodamine (TAMRA, ThermoFisher) for a subset of experiments by following a previously published protocol [72]. 25 mg of TAMRA were first added to a 2.5 mL solution of DMSO and stored at -20 °C in a small eppindorf tube. While being stored, the eppindorf tube was covered with aluminum foil to protect the solution from light. Next, a buffer solution of 0.25 M $NaHCO_3$ and 0.4 M NaCl was made and its pH was adjusted to 9.5 by using a 10M solution of NaOH. After adjusted the pH of this solution, all subsequent steps were performed at 4 °C. We then filled a 1 mL syringe with a 8.46 mg/mL solution of rat tail type 1 collagen in a 0.2N acetic acid solution (Corning) and injected the solution into a 3 mL dialysis cassette. The cassette we used had a 10 kDa molecular weight cutoff. Before retracting the hypodermic needle, we removed air from the cassette by pulling the syringe pump up. We then performed an overnight dialysis in a beaker containg a 1 L solution of our labeling buffer. 100 µL of our 10 mg/mL TAMRA solution was mixed with 900 µL of our labeling buffer, with both solutions at room temperature. After mixing, we placed the TAMRA solution in a 4 °C fridge. The collagen was removed from the cassette using a 2 mL syringe and 1 mL of the solution was mixed with 1 mL of diluted TAMRA using a pipette. The resulting solution was placed in a microcentrifuge tube and incubated with rotation overnight. At this point, the collagen was labeled with the TAMRA dye and this mix was put in a dialysis cassette and dialyzed overnight against a 1 L solution of our labeling buffer. Finally, the TAMRA-labeled collagen was dialyzed overnight against a 0.2% acetic acid solution with a pH of 4. The final volume was recorded to calculate the concentration of the TAMRA-labeled collagen.

3.1.5 Airyscan confocal data preprocessing

Before performing any anlysis on miscropy data from the Zeiss LSM 880 microscopy, image stacks needed to be preprocessed. Raw Carl Zeiss Image (CZI) Airyscan output files from the Zeiss LSM 880 microscope underwent Airyscan processing using Zeiss's imaging software Zen Black. After Airyscan processing, these files were uploaded to FIJI and then exported as .TIFF files. These .TIFF files could then be uploaded to Matlab for further processing.

3.1.6 Automated 3-D cell segmentation, axis length calculation and tracking

A custom automated 2-pass 3-D cell segmentation algorithm coupled with a 3-D tracking algorithm was developed in Matlab for reconstructing and characterizing 3-D cell shapes (Figure 3.1). After preprocessing the Airyscan confocal imaging stacks, the custom algorithm intially uploaded the center z-plane in the stack of the channel containing the labelled dHL-60 cell of interest for the first timepoint in each experiment. A user-defined cell centroid was selected using Matlab's *getpts* function and the *(x y)* coordinates of this point were used to define the centroid of an intial search volume, with dimensions 50 x 50 x 30 pixels^3. The z component of the intial search volume's centroid was defined as the center z-plane in the imaging stack.

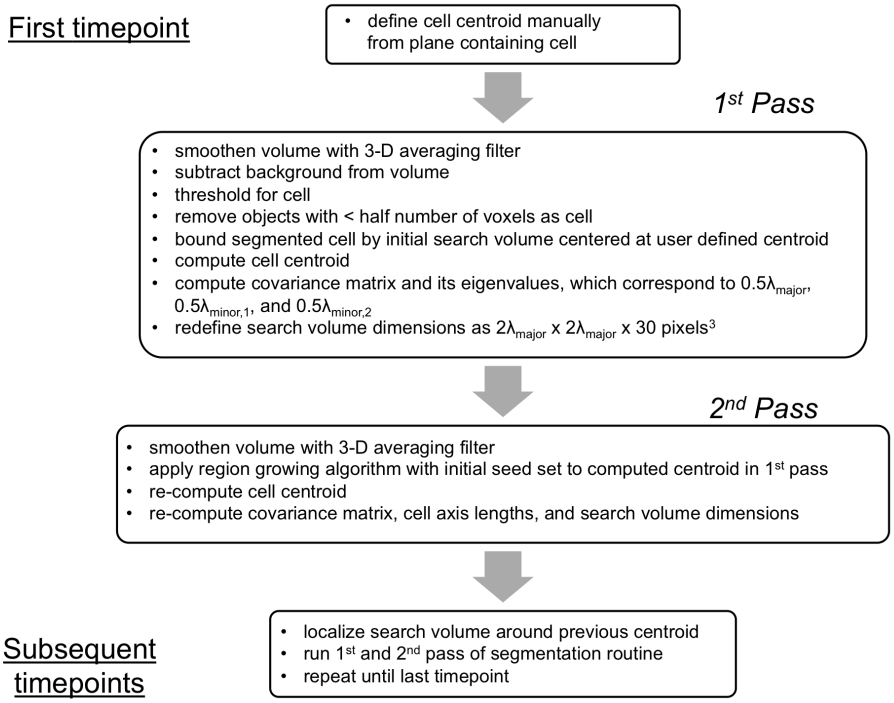

Figure 3.1: Outline of major steps performed in 2-pass segmentation and tracking algorithm for single cell study. The first box contains the steps performed only when analyzing the first timepoint of an experiment. The second two boxes outline the 2-pass segmentation and tracking that is performed for each cell after initial centroids are defined. The last box outlines the subsequent steps, which involve looking in search volumes centered at centroids for each cell at the previous timepoint and performing the 2-pass segmentation and tracking to find the cell's new centroid.

The first pass in the 3-D segmentation and tracking algorithm was performed by uploading the full imaging stack of the labelled cell in the first timepoint and applying an averaging filter with dimensions 3 x 3 x 3 pixels^3 to smoothen the volume. We then subtracted the mean intensity of the volume, which was assumed to be mostly background, from the entire volume. This was done to remove background fluorescence. Assuming that the distribution of intensities in each volume would contain mostly background, we computed the mean of the background subtracted volume and defined a threshold equal to 2 standard deviations from the mean intensity. This threshold represented intensities that were above those found in the background population and thus should belong to the labelled cell. Volumes were binarized with this threshold. To remove small debris that may contain fluorescence in the volume, the number of connected voxels that were calculated using *bwconncomp* and the index number with the largest number of connected voxels was stored. This index corresponded to the segmented cell. Finally, *bwareaopen* was used to remove all objects from the segmented volume with less than half the number of voxels compared to the cell. The resulted segmented image was defined as *I*.

Next, the segmented cell was bounded by the initial search volume, with the user defined centroid, *I(x, y, z)*, being the center of the search volume. Each cell volume, textitV $_{\text{cell}}$, and centroid, *(I $_{c,x}$, I $_{c,y}$, I $_{c,z}$)* was computed using (Eqs. 3.1-3.4), with n number of voxels.

$$V_{cell} = \sum_x \sum_y \sum_z I(x,y,z) \tag{3.1}$$

$$I_{c,x}(x,y,z) = \frac{x_i I(x,y,z)}{V_{cell}} \tag{3.2}$$

$$I_{c,y}(x,y,z) = \frac{y_i I(x,y,z)}{V_{cell}} \tag{3.3}$$

$$I_{c,z}(x,y,z) = \frac{z_i I(x,y,z)}{V_{cell}} \tag{3.4}$$

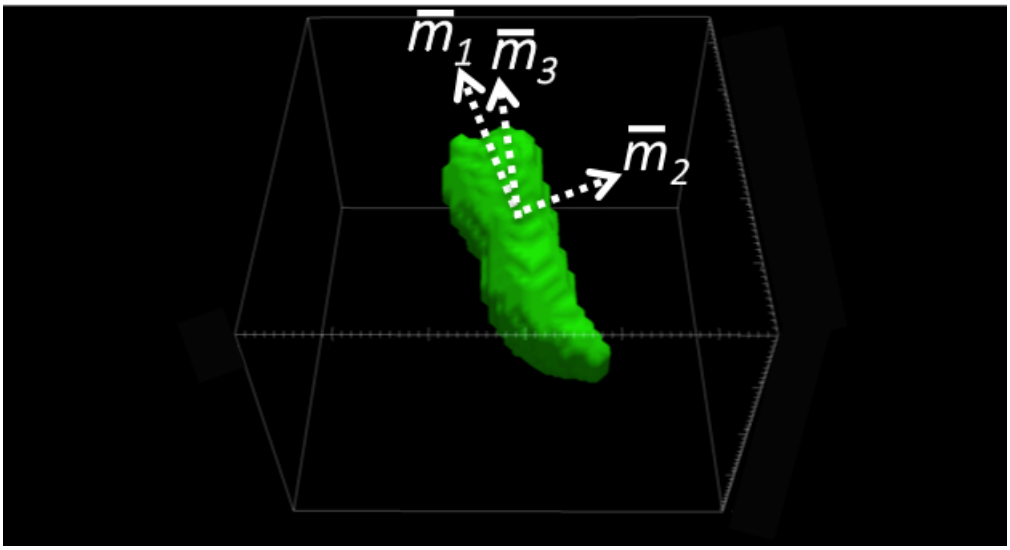

Figure 3.2: Reconstruction of results from coupled automated 3-D cell segmentation and tracking algorithm. Algorithm facilitates the calculation of cells major and two minor cell axes ($\bar{m}_1$, $\bar{m}_2$, and $\bar{m}_3$) show dynamic shape changes during migration.

The image moments of *I(x, y, z)* were computed using (Eq. 3.5-3.10) and used to construct a covariance matrix, $\bar{\bar{I}}_{moment}$ (Eq. 3.11). The eigenvalues of $\bar{\bar{I}}_{moment}$, λ_1, λ_2, and λ_3, corresponded to the cell's axis lengths, with the largest being the major axis length, λ_{major}, and the remained two being minor axis lengths, $\lambda_{minor,1}$ and $\lambda_{minor,2}$ (Eq. 3.7). The principal directions of the cell, $\bar{m}_1$, $\bar{m}_2$, and $\bar{m}_3$, are shown in Figure 3.2. The principal directions of the cell were the eigenvectors of $\bar{\bar{I}}_{moment}$, with the eigenvector that corresponded to the largest eigenvalue being the major axis of the cell.

$$\mu_{200} = \frac{(x_i - I_{c,x})^2 I(x,y,z)}{V_{cell}} \tag{3.5}$$

$$\mu_{020} = \frac{(y_i - I_{c,y})^2 I(x,y,z)}{V_{cell}} \tag{3.6}$$

$$\mu_{002} = \frac{(z_i - I_{c,z})^2 I(x,y,z)}{V_{cell}} \tag{3.7}$$

$$\mu_{110} = \frac{(x_i - I_{c,x})(y_i - I_{c,y}) I(x,y,z)}{V_{cell}} \tag{3.8}$$

$$\mu_{110} = \frac{(x_i - I_{c,x})(z_i - I_{c,z}) I(x,y,z)}{V_{cell}} \tag{3.9}$$

$$\mu_{110} = \frac{(y_i - I_{c,y})(z_i - I_{c,z}) I(x,y,z)}{V_{cell}} \tag{3.10}$$

$$\bar{\bar{I}} = \begin{bmatrix} \mu_{200} & \mu_{110} & \mu_{101} \\ \mu_{110} & \mu_{020} & \mu_{011} \\ \mu_{101} & \mu_{011} & \mu_{002} \end{bmatrix} \tag{3.11}$$

$$eig\left(\bar{\bar{I}}\right) = \begin{bmatrix} \lambda_1 & 0 & 0 \\ 0 & \lambda_2 & 0 \\ 0 & 0 & \lambda_3 \end{bmatrix} \tag{3.12}$$

During a second pass, the full imaging stack of the labelled cell for the first timepoint was smoothened with an averaging filter and segemented again using a 3-D region growing algorithm. This segmentation method worked by starting with an seed with an initial intensity and growing in all directions until intensity values are encountered that are outside of a predetermined range of intensity values. For our data, the initial seed was defined as our computed centroid, *($I_{c,x}$, $I_{c,y}$, $I_{c,z}$)* and we chose to apply a threshold of 90% above and below the initial seed intensity value. This ensured that segmented cells would not have disconnected parts. After obtaining this segmented volume, the cell was bounded by a bounding volume with dimensions $2\lambda_{major}$ x $2\lambda_{major}$ x 30 pixels^3 and cell shape parameters were recalculated from the newly segemented cell.

For the next timepoint, a search volume with dimensions $2\lambda_{major}$ x $2\lambda_{major}$ x 30 pixels^3 was placed in the next timepoint's imaging volume, with its center at the same location as the previously computed centroid after the second segmentation pass. The 2-pass segmentation algorithm was then repeated and a new centroid was computed. This was repeated until the last recorded timelapse volume. It is important to note that the basis of this 3-D segmentation and tracking algorithm relied on the assumption that

were able to image with sufficient temporal resolution to ensure that movements of the cells between timepoints were small enough to be found in neighborhoods around their previous positions. We found this to be the case for our data.

3.1.7 Instantaneous cell velocity

The magnitude of instantaneous cell velocities were computed using Eq 3.13.

$$v(t) = \frac{\|I_c(t+1) - I_c(t)\|_2}{\Delta t} \tag{3.13}$$

3.1.8 Periodicity analysis

Periodicity in the time signals of kinematic parameters such as the cell's major axis length, the mean minor axis length, aspect ratio and the magnitude of instantaneuous cell velocities were analyzed by characterizing the degree of periodicty (*DOP*) in each signal and also performing correlation analysis [38]. The *DOP* was found by first computing the cross correlation of each signal with itself (autocorrelation) and finding the lag T_0 that corresponded to the second highest peak in the resulting autocorrelation. This value represented the period of the time signal. Next, we used the built-in Matlab function *fit* to fit the time signal under analysis with the sine function shown in Eq. 3.14.

$$f(t) = A \sin\left(\frac{2t}{\tau} - \phi\right) \tag{3.14}$$

using T_0 as an initial estimation of the period T. This function was then cross-correlated with the time signal under analysis and multiplied by 100 to obtain the *DOP* (Eq. 3.15).

$$DOP = R_{signal_{sine}} \cdot 100 \tag{3.15}$$

Correlations between the major axis length, mean minor axis length, aspect ratio, and the magnitude of instantaneuous cell velocities were found by subtracting the mean of each signal from the full signal and then performing a cross correlation of the mean subtracted signals with each other.

3.1.9 Cell shape analysis

Cell shape analysis was performed by first randomly selecting 17 timepoints from each experiment. This was a sufficient number of timepoints to obtain random samples for each of the experiments in the collagen gels tested. The major axis length, the mean minor axis length,(Eq. 3.16), and the cell aspect ratio (Eq. 3.17) were then computed for each timepoint in each gel of interest.

$$M.\,Minor\,Axis\,Length = 0.5 \cdot (\lambda_{minor,1} + \lambda_{minor,2}) \tag{3.16}$$

$$M.\,Minor\,Axis\,Length = 0.5 \cdot (\lambda_{minor,1} + \lambda_{minor,2}) \tag{3.17}$$

3.1.10 3-D deformation field

3-D deformation fields, $\bar{u}$ *(u,v,w)* , inside our collagen gels were obtained by using a 2-pass Partice Image Velocity (PIV) approach [73]. The algorithm used was a 2-pass extension of a previously developed 3-D PIV algorithm [74]. Briefly, during a first pass, PIV was performed on each confocal stack of fluorescently labeled beads with respect to the confocal stack of labeled beads for the immediately precending timepoint. An interrogration volume of 56 x 56 x 24 pixels ^{3} with a spacing of 28 x 28 x 22 pixels ^{3} was chosen during this pass. PIV was then ran again using interrogation volumes of 28 x 28 x 22 pixels ^{3} with a spacing of 14 x 14 x 11 pixels ^{3}. During the second pass, the smaller interrogation windows were initially displaced to the regions that were calculated to have

maximum spatial correlations when comparing the confocal stack being anlyzed to the stack at the previous timepoint from the first pass. This resulted is a 3-D deformation field that can capture large deformations due to the relatively large interrogation volumes in the first pass, while also being able to acheive higher spatial resolution from the smaller interrogation volumes used during the second pass.

3.1.11 Deformation field metrics

The magnitude and divergence of the 3-D deformation fields were computed in a traditional manner using Eqs. 3.18-3.19.

$$\| \bar{u} \|_2 = \sqrt{u^2 + v^2 + w^2} \tag{3.18}$$

$$\bigtriangledown \cdot \bar{u} = \frac{\partial u}{\partial x} + \frac{\partial v}{\partial y} + \frac{\partial w}{\partial z} \tag{3.19}$$

3.1.12 3-D cell shape and deformation field metrics reconstructions

3-D reconstructions of cell shapes, deformation fields, and divergence fields were perfomed by first creating Vizualization Toolkit (VTK) files from segmented volumes of the cell at each timepoint, or the computed deformation and divergence fields in Matlab. These files were then imported into the open source software Paraview for 3-D visualization.

3.1.13 Cell-based coordinate system rotations

A 3-D rotation was performed on volumes containing images of cells so that analysis could be performed on the magnitude of deformations and the divergence of those deformation fields in a ”cell-based” coordinate system. After finding the major axis of each cell in each timepoint, we computed azimuthal and polar rotation angles α

and β for rotating our cell by first cropping a region around each cell with dimensions of approximately 36 x 36 x 42 μm ^{3}. This was done for computationally efficiency, considering that we only needed to rotate the cell and its surrounding volume. Next, we creating a 2-D vector $\bar{m}_{3,n}$ comprised of the x and y components of the cell's major axis direction $\bar{m}_3$. The azimuthal angle was computed using these x and y components (Eq. 3.20).

$$\alpha = \tan^{-1}\left(\frac{m_{3,ny}}{m_{3,nx}}\right) \tag{3.20}$$

We then created a 3-D vector in the plane of $\bar{m}_{3,n}$ by computing the magnitude of vectors in directions corresponding to the x and y components of $\bar{m}_{3,n}$, with the z component being 0 (Eq. 3.21).

$$\bar{m_p} = \sqrt{\bar{m_2}^2 + \bar{m_3}^2} \tag{3.21}$$

The polar angle was computed by finding the angle between $\bar{m}_{3,n}$ and $\bar{m}_3$ (Eq. 3.22).

$$\beta = \cos^{-1}\left(\frac{\bar{m_2}}{\bar{m_3})}\right) \tag{3.22}$$

After finding α and β, we performed a 3-D rotation of cells to obtain rotated coordinates (x_{cr}, y_{cr}, z_{cr}) from the original coordinates in our cropped volume ($x_{cr,0}$, $y_{cr,0}$, $z_{cr,0}$) (Eq. 3.23). Finally, we interpolated intensities from our original volume onto the rotated 3-D grid using Matlab's *interp3* function.

$$(x_{cr}\, y_{cr}\, z_{cr}) = [x_{cr,0}\, y_{cr,0}\, z_{cr,0}] \begin{bmatrix} \cos(\alpha) & -\sin(\alpha)\cos(\beta) & \sin(\alpha)\sin(\beta) \\ \sin(\alpha) & \cos(\alpha)\cos(\beta) & -\cos(\alpha)\sin(\beta) \\ 0 & \sin(\beta) & \cos(\beta) \end{bmatrix} \tag{3.23}$$

Each pair of rotation angles (α,β) was also used to rotate deformation fields and the divergence of deformation fields, which were cropped volumes of approximately 46 x 46

x 49 μm ^{3} around the cell's centroid in the corresponding timepoint. The two halves of the cell were separated by splitting the deformation and divergence fields in two according to the front and back halves of the cell. Mean metrics for these two fields were found by computing the average of the field over time and space either within the entire cropped volume or one half of the cropped volume.

3.2 Results

3.2.1 Neutrophils exhibit periodicity during 3-D migration that is independent of matrix density

We began our investigation of cell-matrix interactions and their link to optimal 3-D neutrophil migration by first fluorescently labeled and imaging migrating neutrophil-like cells in our *in-vitro* directed migration assay. The cells were imaged using a confocal microscope under high magnification in order to sufficiently visualize and characterize cell-matrix interactions. We were first interested in whether cells employed periodic or correlated shape changes when migrating in 3-D matrices in a manner similar to what has been described for amoeboid cells during 2-D migration. We were also interested in investigating whether any discernable periodicities or correlated dynamics would be affected by environments with different porosities and densities. Therefore, we utilized our custom 3-D cell segmentation algorithm, coupled with a 3-D cell tracking algorithm to create a tracking volume around each cell in each experiment. Within each tracking volume, we computed the major axis length, λ_{major}, and minor axis lengths, $\lambda_{minor,1}$ and $\lambda_{minor,2}$, of the cell for each timepoint. From these, we computed the aspect ratio of during each timepoint. Given the cells' centroids at each instant of time, I_c, we also were able to compute the magnitude of the cells' instantaneous velocities. The study presented in Chapter 2 illustrated an insignificant different between maximum displacements in the

y direction for cells in 0.25 and 0.5 mg/mL gels and a subsequent significant decrease in maximum displacements with increasing gel concentrations from 0.75 to 2 mg/mL. Given this, we chose to focus our analysis in this study on the three aforementioned concentrations in an attempt to explain the underlying cell-matrix interactions that were responsible for the insignificant difference in migratory behaviors for cells in the two softest and most porous environments as well as the interactions responsible for the different migratory behaviors observed in more dense and stiff environments.

After utlizing our 3-D segmentation and tracking algorithm, we were able to measure kinematic metrics over time (Figure 3.3). We observed qualitatively that cells displayed oscillatory behavior in their axis lengths and movement. This behavior appeared to be present for cells in each of the collagen gels tested as well. To quantify this and check for periodicity, we computed the cross correlation of each signal with a sinusoidal fit of the signal under analysis to explicitely define a degree of periodicity (*DOP*) (Figure 3.4). We found that there was periodicty in the cells' axis lengths, aspect ratios and magnitudes of velocities for each collagen gel concentration tested. Additionally, we found no significant differences between the medians of these *DOP* distributions.

We also analyzed the periods of our time signals by computing the autocorrelation of each signal (Figure 3.5). Results from this analysis showed that periods for these signals were significantly different from 0, while there was no significant difference between the distributions corresponding to different collagen gel concentrations. It is important to note that although there was no statistically significant difference between the medians of cell aspect ratio periods across gel concnetrations, we observed a qualitative increase in this period with increasing collagen gel concentrations.

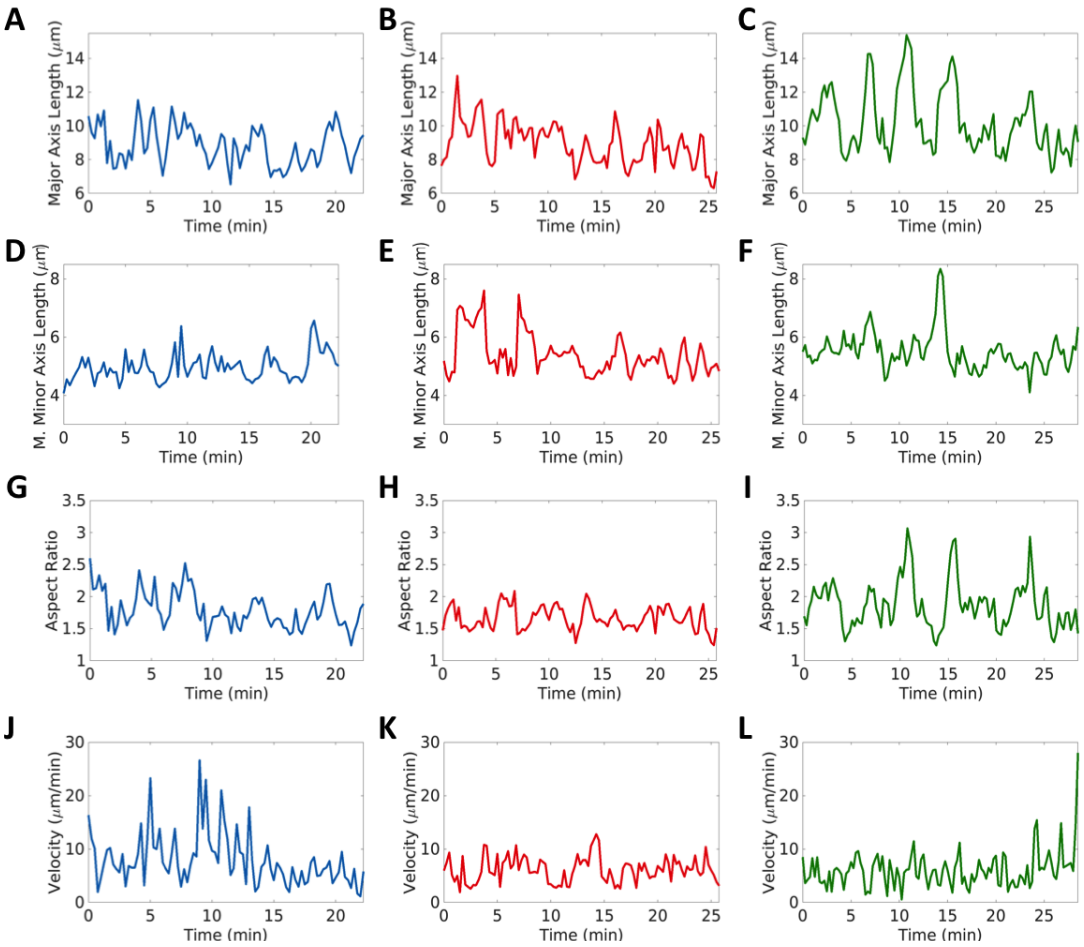

Figure 3.3: Neutrophil shape changes and motion during directed 3-D migration is oscillatory in nature. Representative signals of cell major axis length, mean minor axis length, aspect ratio, and magnitude of cell velocities show oscillations over time in all collagen gel concentrations tested.

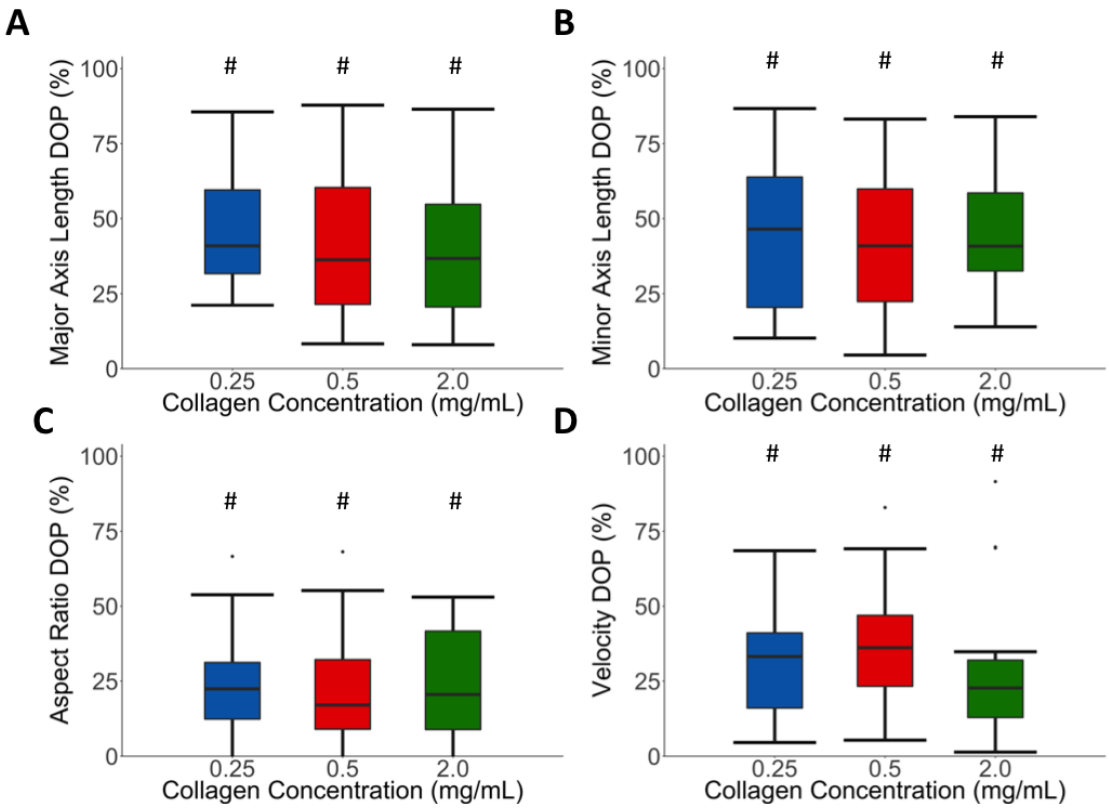

Figure 3.4: Neutrophils engage in periodic cell shape changes and velocity fluctuations that vary in degree during 3-D migration. Median DOP for distributions of cells in 0.25, 0.5, and 2.0 mg/mL collagen gels were significantly different from 0 for changes in the cell's major axis, mean minor axis, aspect ratio, and magnitude of cell velocity. DOP was independent of matrix density for any of the kinematic parameters analyzed. N = 18, 30, and 14 for 0.25, 0.5, and 2.0 mg/mL gels. Wilcoxon signed rank test used to test that median of each distribution is significantly different from 0. # $P < 0.05$. Wilcoxonian rank sum test with Bonferroni correction used to test for significant differences in distribution medians. * $P < 0.01$.

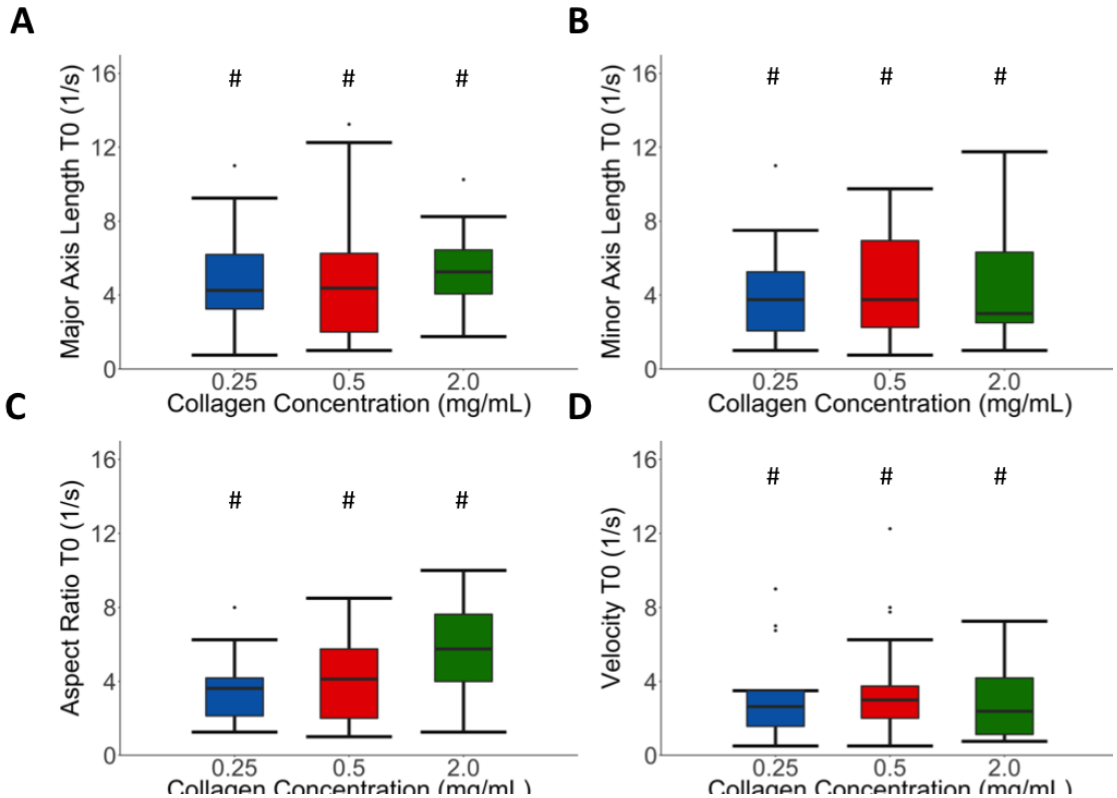

Figure 3.5: Neutrophils migate with similar periodicities in gels with different matrix structures and stiffnesses. Median T0 for distributions of cells in 0.25, 0.5, and 2.0 mg/mL collagen gels were significantly different from 0 for changes in the cell's major axis, mean minor axis, aspect ratio, and magnitude of cell velocity. T0 was independent of matrix density for any of the kinematic parameters analyzed. N = 18, 30, and 14 for 0.25, 0.5, and 2.0 mg/mL gels. Wilcoxon signed rank test used to test that median of each distribution is significantly different from 0. # $P < 0.05$. Wilcoxonian rank sum test with Bonferroni correction used to test for significant differences in distribution medians. * $P < 0.01$.

3.2.2 Neutrophils correlate shape changes and motion in matrix density-dependent manner

Next, we investigated whether any correlations existed between our kinematic parameters and how these correlations may have been affected by the cells' extracellular environments. For the 0.25 mg/mL gels, median correlation coefficients were significantly different from 0 when cross-correlating the cells' mean minor axis length with the cells' velocity magnitude (Figure 3.6). This was similar for cells in 2.0 mg/mL gels. However, median correlation coefficients were significantly different from 0 for cells in 0.5 mg/mL gels when cross-correlating the cells' major axis length with the cells' velocity magnitude. This was also observed between the cells' aspect ratio and velocity magnitude. We found no significant differences between the medians in correlation coefficient distributions across different collagen gel concentrations and no significant correlations existed between major axis length signals and mean minor axis length signals.

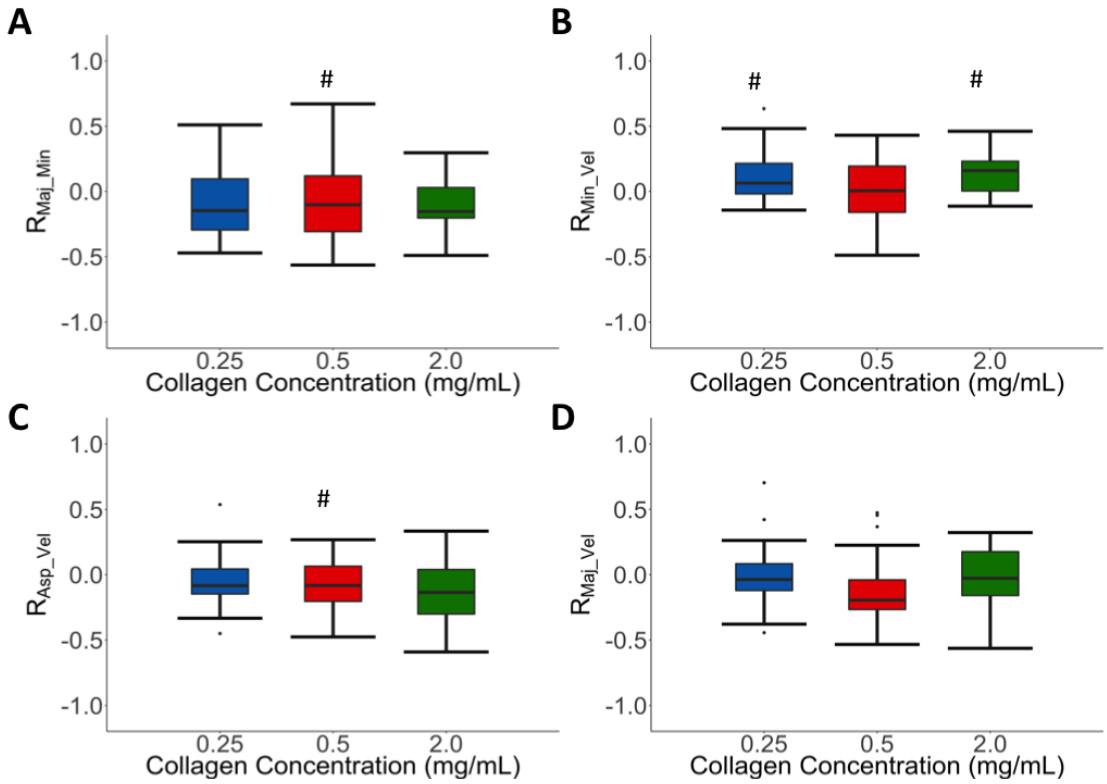

Figure 3.6: Correlation of neutrophil motion and cell shape changes dependent on matrix structure and stiffness. Median R_{Maj_Vel} and R_{Asp_Vel} were only significantly different from 0 for cells in 0.5 mg/mL gels, while median R_{Min_Vel} were significantely different from 0 for cells in 0.25 and 2.0 mg/mL gels. Negative median correlations between cell major axis length and aspect ratio with velocity magnitudes in 0.5 mg/mL gels indicate that cells tend to elongate before moving their center of mass in these environments. Positive median correlations between mean minor axis length and velocity magnitudes in 0.25 and 2.0 mg/mL gels indicate that cells tend to move their center of mass and subsequently increase in width in environments that are porous and soft or dense and stiff. Wilcoxon signed rank test used to test that median of each distribution is significantly different from 0. # $P < 0.05$. Wilcoxonian rank sum test with Bonferroni correction used to test for significant differences in distribution medians. * $P < 0.01$.

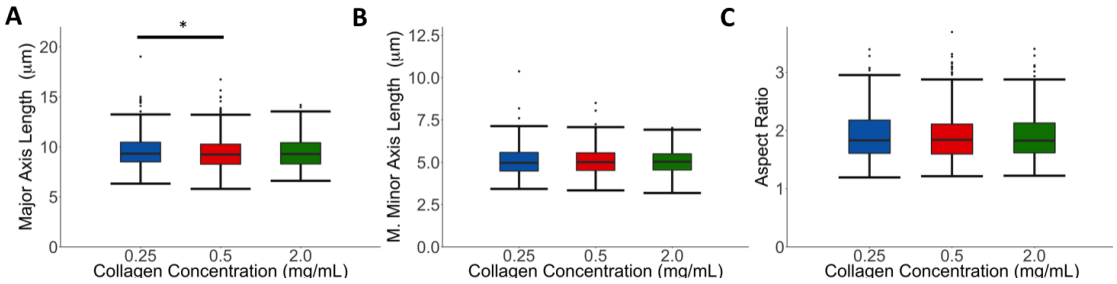

Figure 3.7: Average neutrophil cell shapes are independent of matrix structure and stiffness. Average values for major axis length, minor axis length, and aspect ratio show almost no significant difference across matrices with different densities and mechanical properties tested. 17 randomly selected timepoints for at least 8 cells were used to construct the probability density for each collagen gel concentration. Wilcoxonian rank sum test with Bonferroni correction used to test for significant differences in mean values. text* $P < 0.01$.

3.2.3 Neutrophils adopt similar cell shapes independent of matrix density

We performed cell shape analysis by computing the aforementioned shape metrics during randomly selecting timepoints and pooled data together for cells in similar collagen gel concentrations (Figure 3.7). Results from this analysis show that with the exception of the major axis length, no significant difference exists between the mean values of our cell shape metrics for different types of matrices.

3.2.4 Deformation and divergence field provide insight into cell-matrix interactions

The next type of cell-matrix interactions that we were interested in investigated were the types of forces that migrating neutrophil-like cells exerted on their surrounding matrices. In order study the result of those forces, we examined the 3-D deformation fields around migrating cells using fluorescent microbeads. We first confirmed that the microbeads added to our collagen gels localized to the collagen fibers in our system by fluorescently labeling the reconstituted collagen fibers used for making our gels, fabricating gels without embedded cells, and imaging both the fibers and beads together (Figure 3.8). We saw that beads were exclusively attached to fibers in our system, with no loose beads in the gel's pores.

We then aimed to use confocal stacks of fluorescently labeled beads in our gels to compute deformations inside of our gels. As dHL-60 cells migrated in our extracellular matrices, they applied forces on the matrices which resulted in matrix deformations. This is ilustrated in the timelapse images showing a fluorescently labeled cell with labeled beads in a collagen gel in Figure 3.9. As the cell migrates, neighboring beads displace from their initial postions shown in magenta to their positions in the current timepoint shown in red. These deformations were computing by obtaining the displacement field of the fluorescent microbeads in our system with a 2-pass PIV approach. This gave us the ability to capture large matrix deformations while computing deformations at higher resolutions than would be possible with a 1-pass approach using large interrogation volumes. The confirmation that the fluorescent microbeads were exclusively bound to the collagen fibers gave us confidence that our PIV results were solely a consequence of matrix deformations and not the motion of beads floating in collagen gel pores. Given these deformation fields, we characterized the strength of deformations by computing

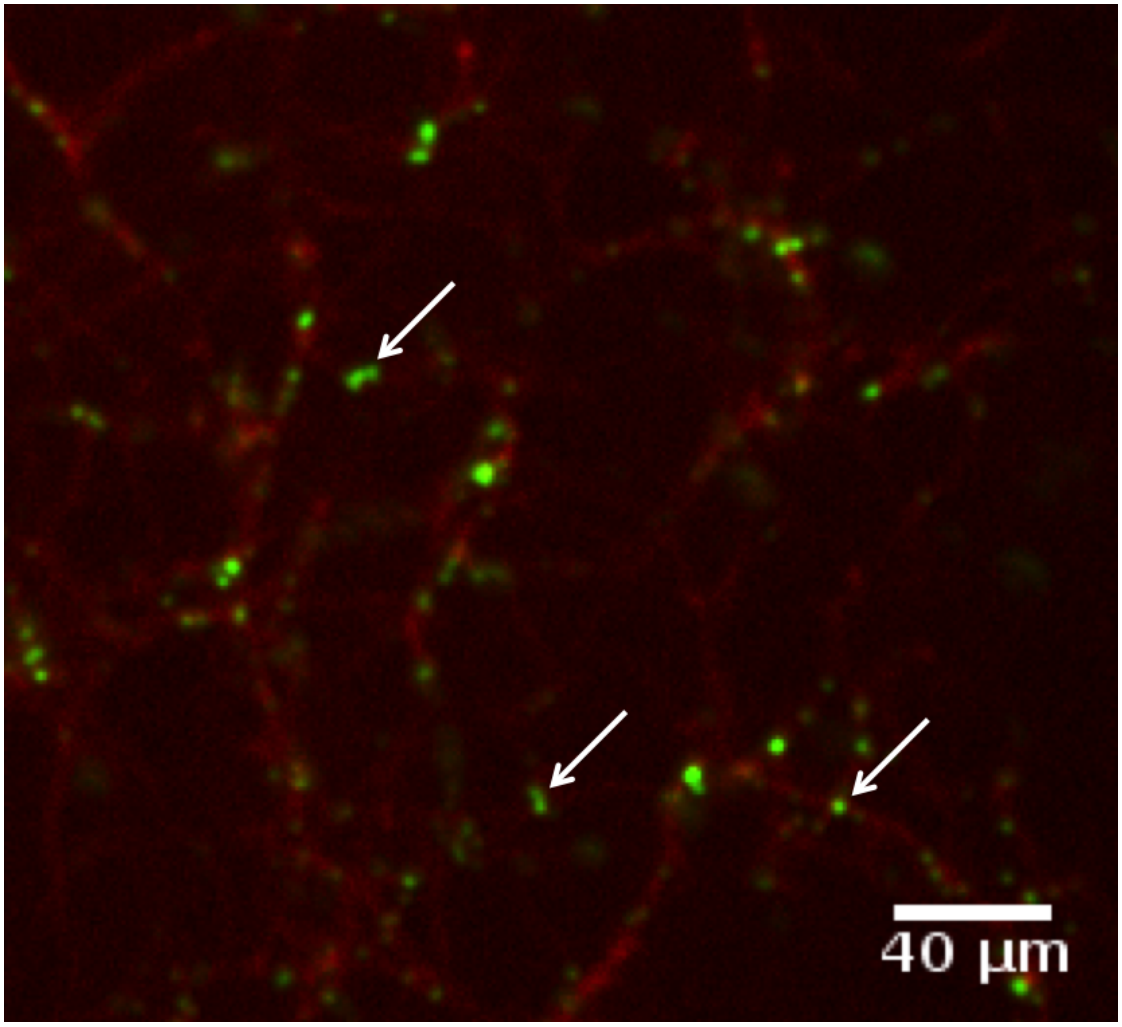

Figure 3.8: Fluorescent microscopy image demonstrating that fluorescent microbeads that were added to collagen gel solutions (green) localize to fluorescently labelled collagen fibers (red) after collagen gel forms. Arrows point to location of beads. Representative image is of 0.5 mg/mL gel collagen gel.

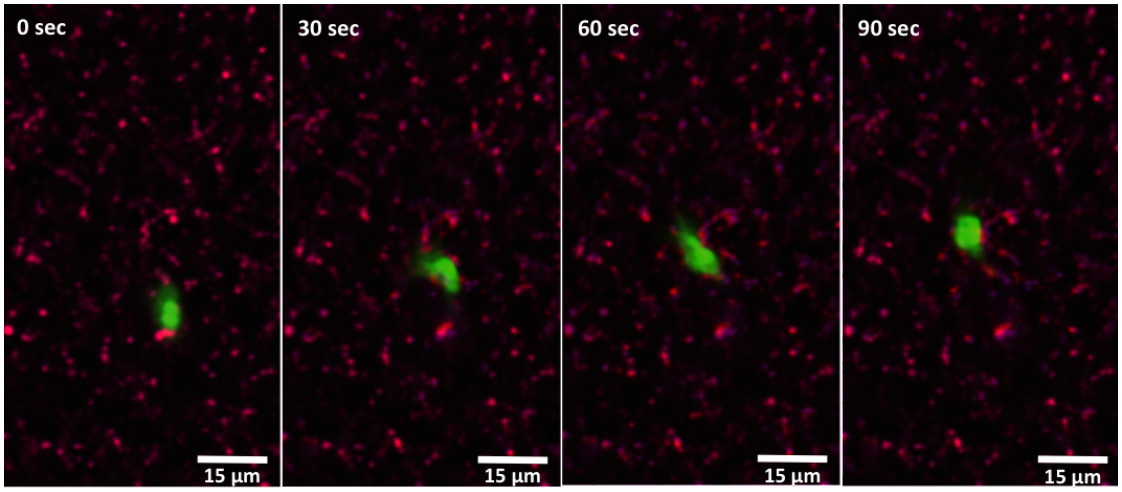

Figure 3.9: Fluorescent microscopy images of labelled dHL-60 cell (green) migrating in 0.5 mg/mL collagen gel with fluorescent microbeads attached to the collagen fibers. Microbeads in the positions observed during the first timepoint are shown in magenta, while microbeads in their positions during each timepoint are shown in red. Forces exerted by dHL-60 cells during migration cause deformations in the collagen matrix, which can be observed by the movement of beads away from their initial positions.

the magnitude of the deformation fields. Additionally, we computed the divergence of the deformation field, which generally quantifies the outward flux of the deformation field from an infinitesimal volume around a source point in the matrix.

Representative examples of our deformation field analysis for the collagen gel concentrations of interest are shown in Figures 3.10-12. The first rows in each figure (Figures 3.10A-E, 3.11A-E, 3.12A-E) contain 3-D reconstructions of migrating dHL-60 cells and fluorescent microbeads in 0.25, 0.5, and 3 mg/mL gels respectively. These reconstructions show that although the distribution of beads in each gel concentration was relatively homogeneous, the bead densities varied, which was related to the decreasing porosity of the collagen gels with increasing collagen concentration.

In Figure 3.10A-E, we see a dHL-60 cell elongate and translocate its center of mass. From the fluorescent images of beads, we computed the deformation and field. Taking the magnitude of the deformation field provided us with a means to characterize instantaneous changes in the strength of the deformations at the timepoints shown in

Figure 3.10A-E (Figure 3.10F-J). This analysis shows us that as the cell elongated, it caused notable changes in deformations that were localized near the cell's front (Figure 3.10G-I). The strength of these changes varied but remained localized over the course of 3 minutes. Also, prominent changes in the strength of deformations occured near the rear of the cell during the last timepoint (Figure 3.10J).

Analysis of the divergence of the deformation field gave us additional insight into the mechanical interactions between neutrophils and collagen matrices (Figure 3.10K-O). The divergence field provides information about the positive flux from an infinetisemal volume around a source point in a material. Therefore, positive values correspond to positive fluxes from a source point while negative values correspond to negative fluxes. In our 0.25 mg/mL experiments, we generally observed both positive and negative fluxes of matrix deformations around the cell. Positive fluxes would typically indicate pulling of matrix material. However, since we analyzed the changes in the divergence field, negative fluxes could either mean that cells were pushing into the matrix or previously stretched matrix material contracted.

Figure 3.10: Analysis of changes in deformation and divergence fields show strength and nature of deformations in matrices during 3-D neutrophil migration in 0.25 mg/mL collagen gels. (A-E) 3-D reconstruction of fluorescent microbeads and cell in gel before migration (A), during elongation (B-D), and during translocation (E). (F-J) 3-D reconstruction of cell and changes in magnitude of deformation fields resulting from forces exerted on matrix by cell during timepoints that correspond to (A-E). Strong changes in matrix deformations observed near front of cell during elongation (G-I) as well as near rear during cell translocation (J). (K-O) Changes in divergence field around migrating cell with blue corresponding to negative matrix material fluxes and red corresponding to positive matrix material fluxes. Strong negative material fluxes were observed around cell shown, especially during elongation and tranlocation events. Chemoattractant source is located in positive y direction and imaging volume was 168 x 168 x 90 μm^3.

A
B
C
D
E
0 min
1 min
2 min
3 min
4 min
F
G
H
I
J
K
L
M
N
O
$\|\bar{u}\|_2$(μm)
2.5
0
$\nabla \cdot \bar{u}$
0.15
-0.15

Figure 3.11: Analysis of changes in deformation and divergence fields show strength and nature of deformations in matrices during 3-D neutrophil migration in 0.5 mg/mL collagen gels. (A-E) 3-D reconstruction of fluorescent microbeads and cell in gel during migration (A-C), and during elongation (B-E). (F-J) 3-D reconstruction of cell and changes in magnitude of deformation fields resulting from forces exerted on matrix by cell during timepoints that correspond to (A-E). Strongest changes in matrix deformations observed near rear of cell during translocation (F-H). (K-O) Changes in divergence field around migrating cell with blue corresponding to negative matrix material fluxes and red corresponding to positive matrix material fluxes. Strong negative material fluxes were observed around the cell shown, especially during elongation tranlocation events. Chemoattractant source is located in positive y direction and imaging volume was 168 x 168 x 90 μm^3.

A
B
C
D
E
0 min
1 min
2 min
3 min
4 min
F
G
H
I
J
K
L
M
N
O
$\|\bar{u}\|_2$ (μm)
2.5
0
$\nabla \cdot \bar{u}$
0.15
-0.15

Figure 3.12: Analysis of changes in deformation and divergence fields show strength and nature of deformations in matrices during 3-D neutrophil migration in 2 mg/mL collagen gels. (A-E) 3-D reconstruction of fluorescent microbeads and cell in gel during migration and elongation (A-E). (F-J) 3-D reconstruction of cell and changes in magnitude of deformation fields resulting from forces exerted on matrix by cell during timepoints that correspond to (A-E). Very weak changes in matrix deformations were observed during migration of cells in these gels (F-J). (K-O) Changes in divergence field around migrating cell with blue corresponding to negative matrix material fluxes and red corresponding to positive matrix material fluxes. Very weak material fluxes were observed around the cell shown. Chemoattractant source is located in positive y direction and imaging volume was 168 x 168 x 90 μm^3.

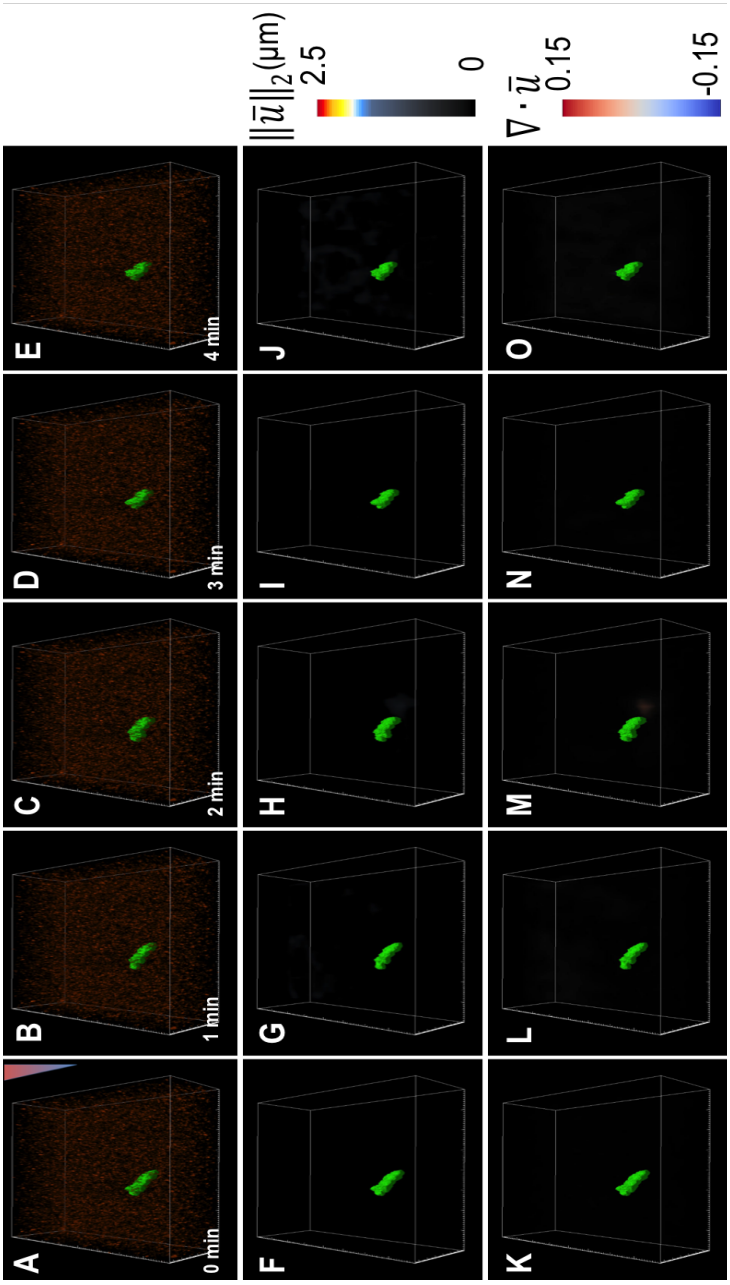
A
B
C
D
E
F
G
H
I
J
K
L
M
N
O
0 min
1 min
2 min
3 min
4 min
$\|\bar{u}\|_2$(μm)
2.5
0
$\nabla \cdot \bar{u}$
0.15
-0.15

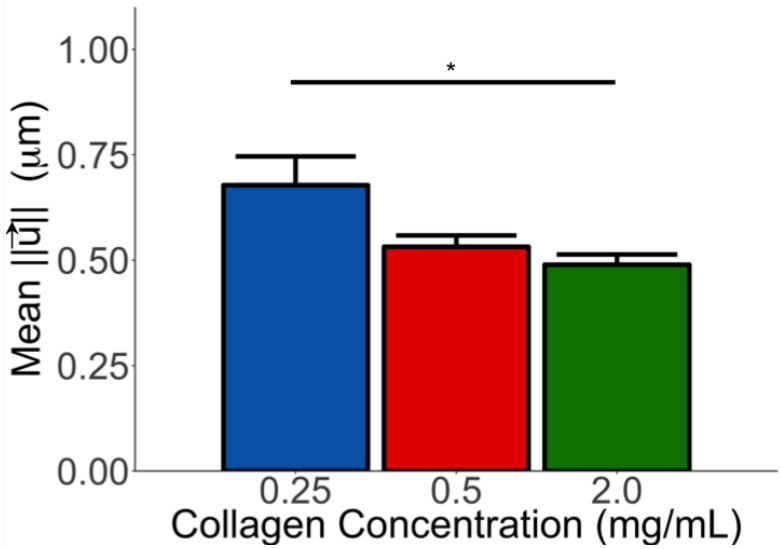

Figure 3.13: Changes in magnitude of deformation field decrease with decreasing matrix density. Qualitatively, magnitude of deformations in volume with dimensions 46 x 46 x 49 μm ^{3} decrease as collagen gel concentration decreases, although significant differences are only observed between 0.25 mg/mL and 2 mg/mL gels. Wilcoxonian rank sum test with Bonferroni correction used to test for significant differences in mean values. * $P < 0.01$.

3.2.5 Cell-matrix interactions appear to be unique to particular matrix densities and mechanical properties

We next aimed to investigate whether changes in deformation fields around migrating dHL-60 cells were unique to particular matrix structures and stiffnesses. To this end, we performed a spatial and temporal averaging of the changes in the magnitude of deformation fields around cells in a bounded volume for our collagen gel concentrations of interest (Figure 3.13). We found that the average change in the magnitude of matrix deformations was 0.678 μm for cells in 0.25 mg/mL, 0.53 μm for cells in 0.5 mg/mL gels and 0.49 μm for cells in 2 mg/mL gels. Although there was a quantitative decrease in the magnitude of deformations with increasing collagen concentration, significant differences only existed between deformations in 0.25 and 2 mg/mL gels.

We were also curious about how push and pull forces were related to directionality during migration. To study the relationship between these forces and directionality, we looked at different components of the divergence of changes in the deformation field (Figure 3.14). For this analysis, we rotated each cell and its divergence field so that they would be orented in a "cell-based" reference frame at each timepoint. This made the comparison between migrating cells in different experiments and gel concentrations easier. We then plotted the center slice of $\frac{\partial \bar{u}}{\partial x}$ along the long axis of the cell and the center slice of $\frac{\partial \bar{v}}{\partial y} + \frac{\partial \bar{w}}{\partial z}$ along the center of the cell, but perpendicular to the long axis of the cell. We found that for each gel concentration, polarity was occasionally evident not only from the elongation of the cell, but from the divergence field, with positive and negative fluxes of the deformation field being localized to the front and back of the cell (Figure 3.14B, E, and H). This is in contrast to the divergence components perpendicular to the long axis of the cell, which were typically apolar with respect to the cell (Figure 3.14C, F, and I).

3.3 Discussion

In this chapter, we aimed to investigate how cell-matrix interactions were linked to the ability of neutrophils to chemotax in a range of environments with different matrix structures and stiffnesses. We were also intersted in determining whether directed 3-D neutrophil migration was linked to unique cell-matrix interactions that depend on the surrounding matrix. We began our investigation with the development of a suite of analysis tools for studying two key aspects of cell-matrix interactions: cell shape changes & motion and matrix deformations. These tools included an automated 3-D cell segmentation algorithm coupled with a 3-D cell tracking algorithm, a workflow for computing 3-D cell shapes, a method for computing the strength and type of 3-D deformations around migrating cells, and a means to easily visualize these events in 3-D.

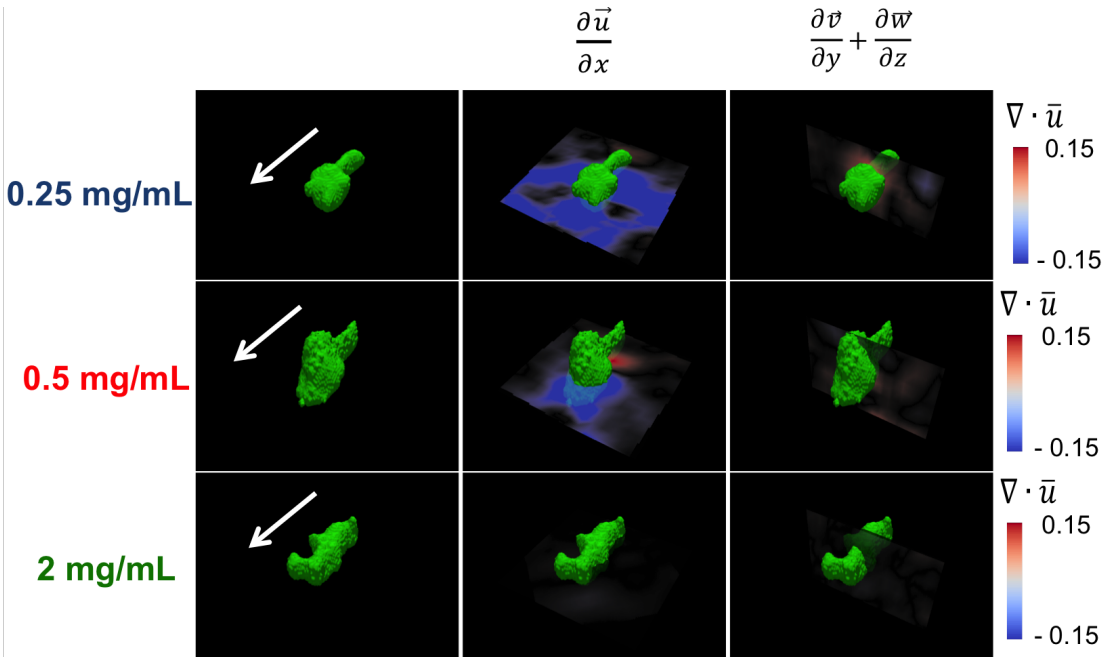

Figure 3.14: Polarization of cell occasionally coincidences with polarization of divergence fields during directed migration. Arrows indicate direction of migration, with pointed end being direction of cell front and blunt end corresponding to back of cell (A, D, G) 3-D reconstruction of polarized dHL-60 cell rotated in "cell-based" coordinate system in 0.25, 0.5, and 2 mg/mL gels, respectively. (B, E, H) 3-D reconstruction of cell with center plane of $\frac{\partial \bar{u}}{\partial x}$, which is the component of the divergence field that is parallel to the long axis of the cell, in 0.25, 0.5, and 2 mg/mL gels. Cells in timepoints shown have polarized divergence fields, with negative deformation fluxes near the front of the cell and positive fluxes near the rear. Also, magnitude of this divergence component decreases with increasing matrix concentration. (C, F, I) 3-D reconstruction of cell with center plane of $\frac{\partial \bar{v}}{\partial y} + \frac{\partial \bar{w}}{\partial z}$, which is the sum of the divergence field components that are perpendicular to the long axis of the cell. This components tended to be nonpolarized when $\frac{\partial \bar{u}}{\partial x}$ was polarized, indicated that the polarization of push and pull forces may be related to directional migration.

When examining one of the two important aspects of cell-matrix interactions, cell shape changes and motion, we were able to observe and quantify periodicty in the major axis length, mean minor axis length, aspect ratio and velocity magnitude during directed 3D migration. The degree of periodicity for neutrophils in collagen gels was similar to that previously reported for *Dictyostelium Discoideum* cells migrating on soft 2-D substrates. Like neutrophils, *Dictyostelium* cells are typically referred to as exhibiting amoeboid motility, with rapid shape changes occuring during migration [27, 75, 28]. The common behavior between these cells may indicate that although directed neutrophils migrate becomes a more complex process when moving from 2-D to 3-D environments, these cells may still attempt to implement a similar intrisic machinery to migrate in a periodic fashion. Interestingly, we were unable to find significant differences in the degree of periodicity across matrices that varied with respect to porosity and stiffness. We were also unable to find significant differences in the periods of motility across the different collagen gels, although qualitative increases in periods of motility were observed with increasing collagen gel concentrations.

Additionally, we examined correlations between the aforementioned kinematic metrics during directed migration and found a significant negative correlation between cells' major axis lengths and velocity magnitudes in gels with intermediate porosities and stiffnesses. This may be related to events of the motility cycle that has been mapped for 2-D amoeboid migration, where during elongatation, the translation of the cell slows down. After the formation of frontal adhesions, these cells may then retract their rear and move their center of mass quicker than during the elongation step. This explanation would account for the negative relationship between major axis lengths and velocity magnitudes for neutrophils in our system.

The aforementioned behavior was not observed in our analysis of cells migrating in gels that were more porose and soft or denser stiff. Instead we found a significant

positive correlation between the cells' mean minor axis lengths and cell velocities. This may also be a feature of some cycle of migration, which would be related to lateral physical interactions with surrounding matrix as cells translate their centers of mass. In porous but soft gels, cells may be engaging in "chimneying" as result of insufficient surrounding matrix matrial. On the other extreme, when migrating through dense gels, cells may simply remain in constant contact with the extracellular matrix and may not need to relie on drastic elongations and frontal adhesions to move forward. Instead, lateral interactions may be sufficient.

During our examination of the dynamics of cell shape and motion changes, we attempted to see if the space of cell shapes explored by neutrophils differed depending on the nature of their surrounding matrix. We were unable to detect differences in most of our cell shape metrics across matrices with different structures and stiffnesses. It was particularly striking that the mean aspect ratio of neutrophil-like cells was similar across the different collagen gels we tested. Previous studies have indicated that as cells migrate through environments with greater confinement, their nuclei tend to become more elongated [59, 76]. We expected that cell shapes would folow a similar trend. Although our result was unexpected, it was significant because it suggests that within limits, neutrophils are able to assume the same necessary shape changes to migrate in different 3-D mechanical environment. This conclusion is consistent with our findings in Chapter 2, which demonstrated that these cells are capable of migrating and chemotaxing in a range of mechanical environments. As an additional confirmation this finding, it would be beneficial to perform this cell shape analysis using 3-D data from imaging modalities with higher spatial resolution. Recent studies have demonstrated that convential confocal microscopy technique are not capable of resolving these cells to capture detailed leuokocyte cell shape features such as pseudopods in the form of thin lamellar sheets and rosettes [77]. Imaging modalities such as lattice light sheet microscopy would

provide sufficient resolution to ensure that our results are not an artifact of not being able to resolve cell features. On a similar note, our shape metrics are computed with the assumption that the cells maintain an ellipsoidal shape during each experiment. This is not always the case. More sophisticated technique and methods for characterizing shapes, such as skeletonization and branch points, could be used as a supplement to our shape analysis to look for more nuanced cell shape differences in environments with different porosities and stiffnesses.

Another key aspect of cell-matrix interactions that we examined were matrix deformations caused by migrating neutrophils. Analysis of 3-D deformation fields showed that strong matrix deformations tend to occur near the front and rear of migrating cells, with stronger deformations being observed in extracellular matrices with higher porosities and lower stiffnesses. Analysis of 3-D divergence fields complemented this and showed that neutrophil-like cells push and possibly pull matrix material matrix material during migration. Negative deformation fluxes, which were associated with pushing forces were observed either near the front or entirely around migrating cells, whereas positive deformation fluxes, which may have been associated with pulling forces, tended to be near the rear of cells when visible. The strength of those pushing and and possible pulling events were stronger in gels with higher porosities and stiffnesses. These results support the idea that pushing and pulling forces are exerted by cells during 3-D neutrophil migration and occur across different types of mechanical environments. As with mean cell shape changes, the similar spatial localization of cell forces during migration may be a common feature that allows these cells to migrate directionally in various mechanical environments. However, our results point to deformation and divergence fields that may have unique features in different environments. To confirm whether the positive deformation fluxes observed are a result of pushing forces, experiments would need to be performed in which a deformation field was obtained by comparing timepoint

sunder analyis with undeformed matrices. This would provide absolute deformations and positive fluxes in the divergence of the deformation field would allow us to say with full confidence that positive deformation fluxes were related to pull forces. This would make sense, given that contractile events have been shown to localize near the near of amoeboid cells during 2-D and 3-D migration. Also, futher quantifications of the divergence field components would be helpful in our investigation into the dynamics of these push and pull forces and thus provide more insight into why these cells chemotax faster in collagen matrices with high porosities and low stiffnesses.

Additionally, actin polymerization and arp 2/3 have been shown to be crucial for pushing forces during 3-D leukocyte migration, while myosin II mediated contractility has been shown to be important for pulling forces [50, 78]. Therefore, follow up studies using our 3-D deformation and divergence field analysis would provide a greater degree of insight into not only cell-matrix interactions with different types of mechanical environments, but the biochemical processes necessary for those interactions and their relationship to directed 3-D neutrophil migration.

Chapter 3, in part, is currently being prepared for submission for publication of the material. François, Joshua, Ayala, Cindy, Yeh, Yi-Ting, del Álamo, Juan Carlos, Lasheras, Juan C. The dissertation author was the primary investigator and author of this material.

Chapter 4

Conclusion

3-dimensional (3-D) leukocyte migration is an extremely complex process that involves the interplay of biochemical signaling events and mechanical interactions between cells and their extracellular environment. Cells must engage their actomyosin machinery when attempting to migrate in 3-D, while responding to the physical landscape in which they are embedded. Environmental factors can include steric hindrance and unique topological structures that may affect how leukocytes choose to migrate.

Although much work has been dedicated to the biochemocal signaling events and pathways that aregulate 3-D leukocyte motility, the role of mechanics in leukocyte migration patterns, cell shape changes and traction force exertion is poorly understood. The work presented in this thesis has aimed to address this deficit by presenting novel experimental and computational tools to study 3-D leukocyte migration in a systematic manner.

The central hypothesis guiding this thesis has been that the structure and stiffness of the extracellular matrix plays a determinant role in directional 3-D neutrophil migration. To investigate this hypothesis, several methodologies were created to gain a

deeper understanding into the mechanics of 3-D neutrophil migration. In Chapter 2, a population study was performed using a custom directed migration device, an automated cell tracking algorithm for 2-D data sets, and a set of metrics to characterize 3-D migration, directionality and persistence. Using these methodologies, we found that although neutrophils were capable of migrating directionally in environments that varied in terms of densities and mechanical properties, these cells demonstrated a stronger chemotactic response in matrices that were of high porosities and low stiffnesses. We also found that the migration of these cells in 3-D fibrous networks can be described as a long memory persistence process. These processes are well described in the field of Statitics. Therefore, this finding opens the door to the possibility of modeling and analyzing this system from a new perspective.

In Chapter 3, we aimed at explaining how cells were able to chemotax in a range of extracellular environments and why they showed a stronger chemotactic response in matrices with the aforementioned optimal densities and mechanical properties by investigating cell-matrix interactions. Specifically, we were interested in understanding how cell shape changes and motion are related to matrix structures and possibly optimal environmental conditions for directed migration. From this study, we found that cells changed their shape in a periodic fashion, although the periodicties of these shape changes did not change with different matrix porosities and stiffnesses. We also found that leukocytes migrating in intermediate porosities and stiffnesses moved with significant negative correlations between their major axis length and velocity, hinting that different kinematic correlations may be needed for migration in different types of matrix environments. Static cell shape analysis demonstrated that cells explored a similar cell shape space across different matrix environments. They also seemed exerted a similar pattern of push and pull forces when migrating in these different environments. This may explain why cells are still able to migrate in environments away from optimal densities

and mechanical properties. However, cells deform their surrounding environments in unique ways that can potentially explain why migration is optimal in particular types of matrices.

Although the focus of this thesis has been on 3-D neutrophil migration, the methodologies developed and results obtained from both studies have the potential to be applied to 3-D migration studies for different types of cell systems. For example, metastatic cancer cells migrate from one location in the body to a distal location in a manner that is somewhat similar to neutrophils. They too transverse environments that range in mechanical composition and properties. The assays and workflows presented could provide additional insight into the limiting environmental factors that affect cancer cell invasion and migration.

Together, the results presented in this thesis demonstrate that directed neutrophil migration in extracellular environments is a robust process that can proceed in different types of environments, within certain limits of matrix density and stiffness. This is consistent with the fact that in physiological conditions, these cells navigate through complex environments that range in porosities and stiffnesses. Nonetheless, an optimal set of environmental factors can make this process occur faster. Additionally, the tools and workflow presented in this work may be applicable to the study of different types of cells in 3-D environments.

Bibliography

[1] Satoshi Kurosaka and Anna Kashina. Cell biology of embryonic migration. *Birth Defects Research Part C: Embryo Today: Reviews*, 84(2):102–122

[2] Andy Aman and Tatjana Piotrowski. Cell migration during morphogenesis. *Developmental biology*, 341(1):20–33

[3] Elena Scarpa and Roberto Mayor. Collective cell migration in development. *J Cell Biol*, 212(2):143–155

[4] Cornelis J Weijer. Collective cell migration in development. *Journal of cell science*, 122(18):3215–3223 2009.

[5] Claudia Tanja Mierke. Physical view on migration modes. *Cell adhesion and migration*, 9(5):367–379

[6] Klaus Ley, Carlo Laudanna, Myron I Cybulsky, and Sussan Nourshargh. Getting to the site of inflammation: the leukocyte adhesion cascade updated. *Nature Reviews Immunology*, 7(9):678

[7] Christine L Chaffer and Robert A Weinberg. A perspective on cancer cell metastasis. *Science*, 331(6024):1559–1564

[8] Tracey A Martin, Lin Ye, Andrew J Sanders, Jane Lane, and Wen G Jiang. Cancer invasion and metastasis: molecular and cellular perspective. 2013.

[9] Denis Wirtz, Konstantinos Konstantopoulos, and Peter C Searson. The physics of cancer: the role of physical interactions and mechanical forces in metastasis. *Nature Reviews Cancer*, 11(7):512

[10] Kwang Hoon Song, Jaehyun Lee, HyoungJun Park, Hye Mi Kim, Jeehun Park, Keon Woo Kwon, and Junsang Doh. Roles of endothelial a-type lamins in migration of t cells on and under endothelial layers. *Scientific Reports*, 6:23412

[11] Elzbieta Kolaczkowska and Paul Kubes. Neutrophil recruitment and function in health and inflammation. *Nature Reviews Immunology*, 13(3):159

[12] Douglas J Goetz, Marwan E El-Sabban, Bendicht U Pauli, and Daniel A Hammer. Dynamics of neutrophil rolling over stimulated endothelium in vitro. *Biophysical journal*, 66(6):2202–2209

[13] Klaus Ley and Thomas F Tedder. Leukocyte interactions with vascular endothelium. new insights into selectin-mediated attachment and rolling. *The Journal of Immunology*, 155(2):525–528

[14] Michael B Lawrence and Timothy A Springer. Leukocytes roll on a selectin at physiologic flow rates: distinction from and prerequisite for adhesion through integrins. *Cell*, 65(5):859–873

[15] Anna C Erickson and John R Couchman. Still more complexity in mammalian basement membranes. *Journal of Histochemistry and Cytochemistry*, 48(10):1291–1306

[16] ACY Li and RPH Basement membrane components, 2003.

[17] Jenny Kruegel and Nicolai Miosge. Basement membrane components are key players in specialized extracellular matrices. *Cellular and Molecular Life Sciences*, 67(17):2879–2895 1420–682X, 2010.

[18] Lewis D Johnson. The biochemical properties of basement membrane components in health and disease. *Clinical biochemistry*, 13(5):204–208

[19] Niels Borregaard. Neutrophils, from marrow to microbes. *Immunity*, 33(5):657–670

[20] Borko Amulic, Christel Cazalet, Garret L Hayes, Kathleen D Metzler, and Arturo Zychlinsky. Neutrophil function: from mechanisms to disease. *Annual review of immunology*, 30:459–489

[21] Alexander Zarbock and Klaus Ley. Mechanisms and consequences of neutrophil interaction with the endothelium. *The American journal of pathology*, 172(1):1–7 2008.

[22] Christopher V Carman and Timothy A Springer. A transmigratory cup in leukocyte diapedesis both through individual vascular endothelial cells and between them. *The Journal of cell biology*, 167(2):377–388 2004.

[23] Samantha L Williams, Ian R Milne, Christopher J Bagley, Jennifer R Gamble, Mathew A Vadas, Stuart M Pitson, and Yeesim Khew-Goodall. A proinflammatory role for proteolytically cleaved annexin a1 in neutrophil transendothelial migration. *The Journal of Immunology*, pages 1000119

[24] Sussan Nourshargh and Ronen Alon. Leukocyte migration into inflamed tissues. *Immunity*, 41(5):694–707

[25] Tim Lämmermann and Michael Sixt. Mechanical modes of 'amoeboid'cell migration. *Current opinion in cell biology*, 21(5):636–644 2009.

[26] Jochen Guck, Franziska Lautenschläger, Stephan Paschke, and Michael Beil. Critical review: cellular mechanobiology and amoeboid migration. *Integrative biology*, 2(11-12):575–583, 2010.

[27] Peter N Devreotes and Sally H Zigmond. Chemotaxis in eukaryotic cells: a focus on leukocytes and dictyostelium. *Annual review of cell biology*, 4(1):649–686 1988.

[28] Masahiro Ueda, Yasushi Sako, Toshiki Tanaka, Peter Devreotes, and Toshio Yanagida. Single-molecule analysis of chemotactic signaling in dictyostelium cells. *Science*, 294(5543):864–867

[29] PR Fisher, Rainer Merkl, and G Gerisch. Quantitative analysis of cell motility and chemotaxis in dictyostelium discoideum by using an image processing system and a novel chemotaxis chamber providing stationary chemical gradients. *The Journal of cell biology*, 108(3):973–984 1989.

[30] Micah Dembo and Yu-Li Wang. Stresses at the cell-to-substrate interface during locomotion of fibroblasts. *Biophysical journal*, 76(4):2307–2316

[31] Myung Eun Shin, Yuan He, Dong Li, Sungsoo Na, Farhan Chowdhury, Yeh-Chuin Poh, Olivier Collin, Pei Su, Primal De Lanerolle, and Martin A Schwartz. Spatiotemporal organization, regulation and functions of tractions during neutrophil chemotaxis. *Blood*, pages blood–2009–12–260851

[32] Lee A Smith, Helim Aranda-Espinoza, Jered B Haun, Micah Dembo, and Daniel A Hammer. Neutrophil traction stresses are concentrated in the uropod during migration. *Biophysical journal*, 92(7):L58–L60

[33] Patrick W Oakes, Dipan C Patel, Nicole A Morin, Daniel P Zitterbart, Ben Fabry, Jonathan S Reichner, and Jay X Tang. Neutrophil morphology and migration are affected by substrate elasticity. *Blood*, 114(7):1387–1395

[34] James P Butler, Iva Marija Tolic-Nørrelykke, Ben Fabry, and Jeffrey J Fredberg. Traction fields, moments, and strain energy that cells exert on their surroundings. *American Journal of Physiology-Cell Physiology*, 282(3):C595–C605

[35] Juan C Del Alamo, Ruedi Meili, Baldomero Alonso-Latorre, Javier Rodríguez-Rodríguez, Alberto Aliseda, Richard A Firtel, and Juan C Lasheras. Spatio-temporal analysis of eukaryotic cell motility by improved force cytometry. *Proceedings of the National Academy of Sciences*, 104(33):13343–13348

[36] Juan C Del Álamo, Ruedi Meili, Begoña Álvarez-González, Baldomero Alonso-Latorre, Effie Bastounis, Richard Firtel, and Juan C Lasheras. Three-dimensional

quantification of cellular traction forces and mechanosensing of thin substrata by fourier traction force microscopy. *PloS one*, 8(9):e69850

[37] Ruedi Meili, Baldomero Alonso-Latorre, Juan C Del Álamo, Richard A Firtel, and Juan C Lasheras. Myosin ii is essential for the spatiotemporal organization of traction forces during cell motility. *Molecular biology of the cell*, 21(3):405–417 2010.

[38] Effie Bastounis, Ruedi Meili, Baldomero Alonso-Latorre, Juan C del Álamo, Juan C Lasheras, and Richard A Firtel. The scar/wave complex is necessary for proper regulation of traction stresses during amoeboid motility. *Molecular biology of the cell*, 22(21):3995–4003 2011.

[39] Leo Boneschansker, Jun Yan, Elisabeth Wong, David M Briscoe, and Daniel Irimia. Microfluidic platform for the quantitative analysis of leukocyte migration signatures. *Nature communications*, 5:4787

[40] Yan-Jun Liu, Maël Le Berre, Franziska Lautenschlaeger, Paolo Maiuri, Andrew Callan-Jones, Mélina Heuzé, Tohru Takaki, Raphaël Voituriez, and Matthieu Piel. Confinement and low adhesion induce fast amoeboid migration of slow mesenchymal cells. *Cell*, 160(4):659–672

[41] Lena A Lautscham, Christoph Kämmerer, Janina R Lange, Thorsten Kolb, Christoph Mark, Achim Schilling, Pamela L Strissel, Reiner Strick, Caroline Gluth, and Amy C Rowat. Migration in confined 3d environments is determined by a combination of adhesiveness, nuclear volume, contractility, and cell stiffness. *Biophysical journal*, 109(5):900–913

[42] Bryan Heit and Paul Kubes. Measuring chemotaxis and chemokinesis: the under-agarose cell migration assay. *Sci. STKE*, 2003(170):pl5–pl5

[43] Robert D Nelson, Paul G Quie, and Richard L Simmons. Chemotaxis under agarose: a new and simple method for measuring chemotaxis and spontaneous migration of human polymorphonuclear leukocytes and monocytes. *The Journal of Immunology*, 115(6):1650–1656 1975.

[44] Stephanie Toetsch, Peter Olwell, Adriele Prina-Mello, and Yuri Volkov. The evolution of chemotaxis assays from static models to physiologically relevant platforms. *Integrative Biology*, 1(2):170–181, 2009.

[45] Michael Sixt and Tim Lämmermann. *In vitro analysis of chemotactic leukocyte migration in 3D environments*, pages 149–165. Springer, 2011.

[46] Ulrike Haessler, Marco Pisano, Mingming Wu, and Melody A Swartz. Dendritic cell chemotaxis in 3d under defined chemokine gradients reveals differential response to ligands ccl21 and ccl19. *Proceedings of the National Academy of Sciences*, 108(14):5614–5619

[47] G Pagano, M Ventre, M Iannone, F Greco, PL Maffettone, and PA Netti. Optimizing design and fabrication of microfluidic devices for cell cultures: An effective approach to control cell microenvironment in three dimensions. *Biomicrofluidics*, 8(4):046503

[48] O Moreno-Arotzena, G Mendoza, M Cóndor, T Rüberg, and JM García-Aznar. Inducing chemotactic and haptotactic cues in microfluidic devices for three-dimensional in vitro assays. *Biomicrofluidics*, 8(6):064122

[49] Christian Frantz, Kathleen M Stewart, and Valerie M Weaver. The extracellular matrix at a glance. *J Cell Sci*, 123(24):4195–4200

[50] Wolfgang Weninger, Maté Biro, and Rohit Jain. Leukocyte migration in the interstitial space of non-lymphoid organs. *Nature Reviews Immunology*, 14(4):232

[51] Tim Lämmermann and Ronald N Germain. *The multiple faces of leukocyte interstitial migration*, volume 36. Springer, 2014.

[52] Tim Lämmermann, Bernhard L Bader, Susan J Monkley, Tim Worbs, Roland Wedlich-Söldner, Karin Hirsch, Markus Keller, Reinhold Förster, David R Critchley, and Reinhard Fässler. Rapid leukocyte migration by integrin-independent flowing and squeezing. *Nature*, 453(7191):51

[53] Bettina Weigelin, Gert-Jan Bakker, and Peter Friedl. Intravital third harmonic generation microscopy of collective melanoma cell invasion: principles of interface guidance and microvesicle dynamics. *IntraVital*, 1(1):32–43

[54] Elizabeth M Culav, C Heather Clark, and Mervyn J Merrilees. Connective tissues: matrix composition and its relevance to physical therapy. *Physical therapy*, 79(3):308–319

[55] Allison R Gillies and Richard L Lieber. Structure and function of the skeletal muscle extracellular matrix. *Muscle and nerve*, 44(3):318–331

[56] Stephanie I Fraley, Pei-hsun Wu, Lijuan He, Yunfeng Feng, Ranjini Krisnamurthy, Gregory D Longmore, and Denis Wirtz. Three-dimensional matrix fiber alignment modulates cell migration and mt1-mmp utility by spatially and temporally directing protrusions. *Scientific reports*, 5:14580

[57] DO Velez, B Tsui, T Goshia, CL Chute, A Han, H Carter, and SI Fraley. 3d collagen architecture induces a conserved migratory and transcriptional response linked to vasculogenic mimicry. *Nature communications*, 8(1):1651

[58] Muhammad H Zaman, Linda M Trapani, Alisha L Sieminski, Drew MacKellar, Haiyan Gong, Roger D Kamm, Alan Wells, Douglas A Lauffenburger, and Paul Matsudaira. Migration of tumor cells in 3d matrices is governed by matrix stiffness

along with cell-matrix adhesion and proteolysis. *Proceedings of the National Academy of Sciences*, 103(29):10889–10894

[59] Katarina Wolf, Mariska Te Lindert, Marina Krause, Stephanie Alexander, Joost Te Riet, Amanda L Willis, Robert M Hoffman, Carl G Figdor, Stephen J Weiss, and Peter Friedl. Physical limits of cell migration: control by ecm space and nuclear deformation and tuning by proteolysis and traction force. *J Cell Biol*, 201(7):1069–1084

[60] Arthur Millius and Orion D Weiner. *Chemotaxis in neutrophil-like HL-60 cells*, pages 167–177. Springer, 2009.

[61] Stefan Münster and Ben Fabry. A simplified implementation of the bubble analysis of biopolymer network pores. *Biophysical journal*, 104(12):2774–2775

[62] Wayne W Daniel. *Biostatistics: A Foundation for Analysis in the Health Sciences (Probability and Mathematical Statistics)*. John Wiley and Sons, New York, 1987.

[63] Philippe V Afonso, Colin P McCann, Senta M Kapnick, and Carole A Parent. Discoidin domain receptor 2 regulates neutrophil chemotaxis in 3d collagen matrices. *Blood*, pages blood–2012–08–451575

[64] Tim Lämmermann, Bernhard L Bader, Susan J Monkley, Tim Worbs, Roland Wedlich-Söldner, Karin Hirsch, Markus Keller, Reinhold Förster, David R Critchley, and Reinhard Fässler. Rapid leukocyte migration by integrin-independent flowing and squeezing. *Nature*, 453(7191):51

[65] Steven J Collins, Francis W Ruscetti, Robert E Gallagher, and Robert C Gallo. Terminal differentiation of human promyelocytic leukemia cells induced by dimethyl sulfoxide and other polar compounds. *Proceedings of the National Academy of Sciences*, 75(5):2458–2462

[66] Jeremy Keys, Aaron Windsor, and Jan Lammerding. *Assembly and Use of a Microfluidic Device to Study Cell Migration in Confined Environments*, pages 101–118. Springer, 2018.

[67] Julian Steinwachs, Claus Metzner, Kai Skodzek, Nadine Lang, Ingo Thievessen, Christoph Mark, Stefan Münster, Katerina E Aifantis, and Ben Fabry. Three-dimensional force microscopy of cells in biopolymer networks. *Nature methods*, 13(2):171

[68] Ruedi Meili, Baldomero Alonso-Latorre, Juan C Del Álamo, Richard A Firtel, and Juan C Lasheras. Myosin ii is essential for the spatiotemporal organization of traction forces during cell motility. *Molecular biology of the cell*, 21(3):405–417 2010.

[69] Jan *Statistics for long-memory processes*. Routledge, 2017.

[70] Paul Doukhan, George Oppenheim, and Murad *Theory and applications of long-range dependence*. Springer Science and Business Media, 2002.

[71] DD Hickstein, Anthony L Back, and Steven J Collins. Regulation of expression of the cd11b and cd18 subunits of the neutrophil adherence receptor during human myeloid differentiation. *Journal of Biological Chemistry*, 264(36):21812–21817 0021–9258, 1989.

[72] Sara Geraldo, Anthony Simon, and Danijela M Vignjevic. Revealing the cytoskeletal organization of invasive cancer cells in 3d. *Journal of visualized experiments: JoVE*, (80), 2013.

[73] Markus Raffel, Christian E Willert, Fulvio Scarano, Christian J Kähler, Steve T Wereley, and Jürgen *Particle image velocimetry: a practical guide*. Springer, 2018.

[74] Yi-Ting Yeh, Ricardo Serrano, Joshua François, Jeng-Jiann Chiu, Yi-Shuan Julie Li, Juan C del Álamo, Shu Chien, and Juan C Lasheras. Three-dimensional forces exerted by leukocytes and vascular endothelial cells dynamically facilitate diapedesis. *Proceedings of the National Academy of Sciences*, pages 201717489

[75] William *Dictyostelium discoideum: a developmental system*. Elsevier, 2012.

[76] Lena A Lautscham, Christoph Kämmerer, Janina R Lange, Thorsten Kolb, Christoph Mark, Achim Schilling, Pamela L Strissel, Reiner Strick, Caroline Gluth, and Amy C Rowat. Migration in confined 3d environments is determined by a combination of adhesiveness, nuclear volume, contractility, and cell stiffness. *Biophysical journal*, 109(5):900–913

[77] Lillian K Fritz-Laylin, Megan Riel-Mehan, Bi-Chang Chen, Samuel J Lord, Thomas D Goddard, Thomas E Ferrin, Susan M Nicholson-Dykstra, Henry Higgs, Graham T Johnson, and Eric Betzig. Actin-based protrusions of migrating neutrophils are intrinsically lamellar and facilitate direction changes. *Elife*, 6:e26990

[78] Alexander Leithner, Alexander Eichner, Jan Müller, Anne Reversat, Markus Brown, Jan Schwarz, Jack Merrin, David JJ de Gorter, Florian Schur, and Jonathan Bayerl. Diversified actin protrusions promote environmental exploration but are dispensable for locomotion of leukocytes. *Nature cell biology*, 18(11):1253